Oberlin

[Digital Commons at Oberlin](https://digitalcommons.oberlin.edu)

2011

Infrared Spectroscopy of Trapped Gases in Metal-Organic Frameworks

Jennifer M. Schloss
Oberlin College

Follow this and additional works at: https://digitalcommons.oberlin.edu/honors

Part of the Physics Commons

Infrared Spectroscopy of Trapped Gases in Metal-Organic Frameworks

Jennifer M. Schloss

Department of Physics and Astronomy

Oberlin College

Honors Thesis

April 8, 2011

Acknowledgements

I would like to thank my advisor, Professor Stephen FitzGerald, for his patient guidance, teaching, and encouragement. He has been a valuable mentor to me throughout my college career, and during this project in particular I have benefitted tremendously from his wisdom.

I also owe many thanks to Professor Jesse Rowsell for synthesizing the materials studied in this lab and for helpful insights and advice.

I wish to thank my lab mates Chris Pierce, Ben Thompson, and Dan Ljungberg for their company and hard work in the lab.

I am much indebted to Professor Fitzgerald's previous Honors students, especially to Jesse Hopkins and Michael Friedman, for laying the groundwork for my Honors project and for their clearly-written, informative theses.

I am grateful to Bill Marton, for machining many parts of our apparatus, and to Bill Mohler, for his electronics expertise and for fixing our spectrometer multiple times.

I would like to thank the Oberlin College Department of Physics and Astronomy for giving me an excellent education and for providing me with the opportunity and the resources to complete this undertaking.

Thanks to Jacob Baron for his patience and advice and for being my sounding board. I owe many thanks also to Laura Tully-Gustafson, Ryan Head, and all of my friends for their encouragement and for keeping me balanced. Finally, I never would have had this experience or completed this project without the support of my family, to whom I am incredibly grateful.

Contents

List of Figures

LIST OF FIGURES

List of Tables

LIST OF TABLES

Executive Summary

There are a range of environmental and industrial applications to capturing carbon dioxide from gas mixtures. Currently, materials being used in these applications bind carbon dioxide too strongly for practical purposes, such that they require large amounts of energy to be regenerated for reuse.

Highly porous materials called metal-organic frameworks (MOFs) could serve much more effectively as carbon-capturing materials, as they suck up large amounts of carbon dioxide gas at pressures and temperatures that are nearly ideal for carbon-capture applications. Moreover, they require much less energy than current materials to release the carbon dioxide and be regenerated. Additionally, many different structures can be created fairly easily, so scientists are on the hunt for the ideal carbon-capturing MOF.

In this thesis we study Mg-MOF-74, a particularly promising metal-organic framework material for separating carbon dioxide from gas mixtures. We use infrared spectroscopy to probe the interactions between the Mg-MOF-74 host and both carbon dioxide and methane. By shining infrared radiation on Mg-MOF-74 with gases trapped in it and looking at which frequencies of radiation are absorbed by the bound gases, we can learn about the binding nature of the framework. This in turn helps us to better understand the properties are are preferable in metal organic frameworks, and will aid chemists in fabricating new structures that are ideal for carbon-capture and other applications.

0. EXECUTIVE SUMMARY

1

Introduction

1.1 Motivation

As global temperatures have been rising over the past century, so have atmospheric concentrations of greenhouse gases. A large and growing body of evidence links these two phenomena and attributes the increased greenhouse gas levels to human activity, specifically to the burning of fossil fuels (1). Carbon dioxide, the primary greenhouse gas emitted in fuel combustion, is at its highest atmospheric concentration in 650,000 years and continues to rise (1). Among the effects of the planet's changing climate are destruction of ecosystems and increased flooding of coastal regions (2). In order to combat these changes and to ensure that the earth will continue to support life in the future, humans must reduce greenhouse gas emissions.

In response to this global climate crisis, there has been much effort devoted to developing alternative energy technologies. Emissions reduction requires a multipronged approach, ultimately involving a switch away from fossil fuels, although realistically a complete switch to clean energy sources will take years. In the mean time, methods to mitigate the harmful effects of fossil fuel combustion are needed. In particular, technologies for carbon capture and storage (CCS) are being developed to reduce CO_2-emissions.

CCS consists of separating CO_2 from exhaust gas streams, compressing it, and injecting it into geologic structures in the earth. Of the multiple steps in the CCS process, separating CO_2 from exhaust gases, also called flue gases, is the most costly (3). Current technologies involve scrubbing with amines, in which CO_2 in a flue gas

1. INTRODUCTION

mixture reacts with an aqueous amine solution. CO_2-rich solution is then removed from the solvent via heating, and in principle the amines are regenerated (2).

Amine-scrubbing is the best-understood CO_2-separation method and has been in practice for over 60 years (4). The process, however, uses significant amounts of energy to remove CO_2 and regenerate the solvents. It is also both costly and harmful, as trace flue gases can degrade the amine solvents, and amines are corrosive (2). There-fore, there has been a push to develop alternative methods for separating CO_2 from gas mixtures. Recently, a different class of material is receiving attention for CCS applications. Metal-organic frameworks (MOFs) are extremely porous structures with record-breaking surface areas and high affinities for binding gases to their surfaces (2, 5, 6, 7, 8, 9, 10). They have the highest known storage densities for carbon dioxide, methane, cryogenic diatomic hydrogen (2). Their structure and adsorption properties will be discussed further in § 1.2.

MOFs are promising candidates for use in CO_2 separation and capture technologies, as they have been shown to selectively bind CO_2 over other gases including nitrogen and methane (2). Since metal-organic frameworks can be easily modified, a variety of different structures have been fabricated. This thesis focuses in particular on a framework with the name MOF-74. This MOF is especially promising for CCS appli-cations because it has a particularly high selectivity for binding carbon dioxide over other gases. MOF-74 has an especially high CO2-affinity at low pressures and ambient temperatures, which makes it one of the best MOFs fabricated thus far for separating CO_2 from gas mixtures, because typical CO_2-concentrations in flue gases are low, at 4-12 percent volume (11).

In addition to CCS, there is interest in employing MOFs in the processing of natu-ral gas prior to combustion, to remove carbon dioxide from methane streams. Natural gas with methane as its main component also contains CO_2 and other impurities that reduce the energy content of the gas and can lead to corrosion of pipelines (12). Thus an important step in natural gas processing is the removal of CO_2. Cryogenic distilla-tion is commonly used for this step, in which the gas mixture is cooled to freeze out CO_2 and other impurities. However, separation methods that run at or near ambient temperatures are often preferable to cryogenic distillation as they are less costly, more energy efficient, and easier to control (12). Selective adsorption of carbon dioxide onto

porous materials is one such promising gas-separation method. In the past, aluminosilicate materials called zeolites have been used as the adsorbents, although MOFs have received attention in recent years as a family of materials with promise for use in gas separation because of their CO_2-uptakes and because the can be regenerated under milder conditions than most zeolites (12).

Metal-organic frameworks also show promise as hydrogen-storage hosts, although current MOFs in existence bind H_2 too weakly to be viable hosts at ambient temperatures and pressures. Still, must research is being done into the hydrogen-storage properties of MOFs (6, 7, 8, 13, 14, 15, 16, 17, 18). The Oberlin College Honors theses of Jesse Hopkins, Brian Burkholder, and Michael Friedman report on infrared spectroscopy of hydrogen in a range of MOFs (19, 20, 21), and their results can help direct the search for MOFs that are practical for hydrogen storage applications.

There is still much to be learned about metal-organic framework structures and the nature of the binding mechanism of CO_2 and other gases to their surfaces. The work presented in this thesis has two overarching goals. The first is to probe through infrared spectroscopy the nature of the interactions between adsorbed gases and the particular MOFs we study. Specifically, we focus on CO_2 in Mg-MOF-74 because of the promise of that particular MOF in CCS applications and in separating CO_2 from natural gas streams.

The second goal is to gain a better understanding the electronic environments within MOFs in general so that theoretical models can more accurately predict the properties of these structures. We aim to use the adsorbed molecules as probes to measure the electric field at locations within MOFs. This information can be used to calibrate theoretical models so that they better predict the structures and compositions of new MOFs. Reliable models would give chemists direction in fabricating MOFs with ideal adsorption capacities for a variety of applications ranging from CCS and gas separation to hydrogen storage.

1.2   MOF-74

Metal-organic frameworks, which typically exist in crystalline powder form, consist of metal-oxide clusters linked together by organic bridging ligands to form a three-dimensional repeating structures. Solvent molecules are evacuated from the MOF pores

leaving open surfaces for gas molecules to bind to(2). The binding of gas molecules to the framework surfaces is termed adsorption. As noted in the previous section, MOFs have high gas-storage capacities and potential applications to gas separation and hydrogen-storage for fuel cells.
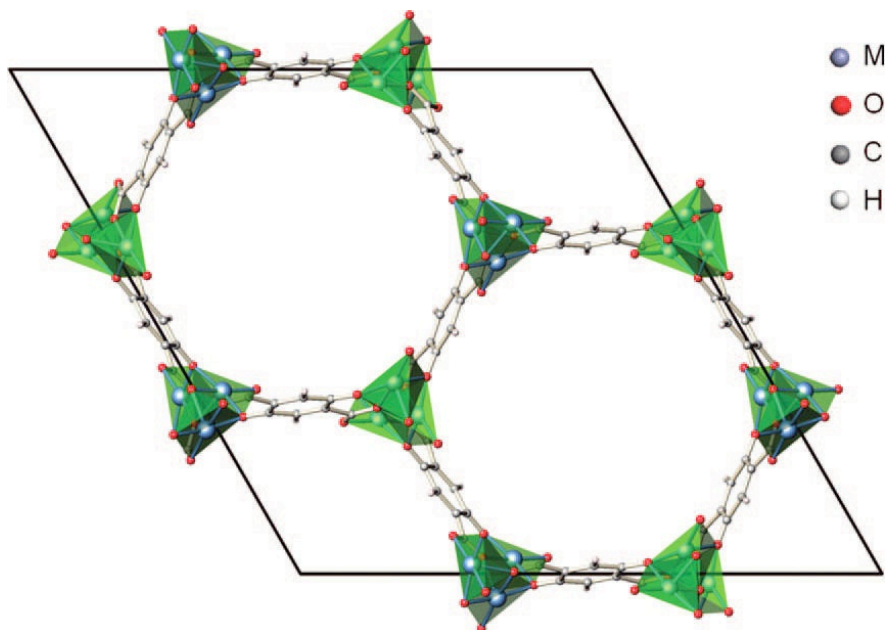
Figure 1.1: The MOF-74 structure, from neutron diffraction data taken by Wu et al. (22) - The framework consists of metal-oxide clusters bound by organic linkers to form a honeycomb-like structure with infinite hexagonal channels. When the framework is activated and solvent molecules are removed, the coordination metals occupying the corners of the hexagons are bound to five ligands and have one binding site open.

In this thesis we focus on a particular metal-organic framework structure termed MOF-74, which has one of the largest gas-uptake capacities yet observed (15, 17). MOF-74 consists of metal-oxide clusters bound by organic linkers to form a honeycomb-like structure with infinite hexagonal channels into which gases can diffuse. Figure 1.1 shows the framework structure. We refer to the coordination metals occupying the corners of the hexagons as open or exposed metal ions because when the framework is activated and solvent molecules are removed, each metal, which is in a 2^+ oxidation state, is bound to five ligands and has one binding site open.

The first MOF-74 sample created contained zinc as the metal ion, although in subsequent years a range of MOF-74 species have been fabricated with different co-

ordination metals including magnesium, manganese, cobalt, and nickel. We refer to individual members of the isostructural series by the name M-MOF-74, where M represents whichever metal is substituted in to the framework.

The MOF-74 species with the highest CO_2-affinity is Mg-MOF-74, for reasons that are not yet fully understood but which we will discuss in Chapter 4. In this thesis we focus the bulk of our study on CO_2 in Mg-MOF-74. We compare the CO_2-adsorption properties of Mg-MOF-74 to those of three other MOFs in the isostructural series, namely Mn-, Co-, and Zn-MOF-74. We also compare CO_2 to CH_4 adsorbed to Mg-MOF-74, as gas separation applications of Mg-MOF-74 would include selectively binding CO_2 over CH_4 in natural gas streams.

1.3   Infrared spectroscopy

To probe the interactions between the adsorbed gas and the MOF host we use Fourier transform infrared spectroscopy (FTIR). In our setup, infrared radiation strikes a sample of MOF-74 loaded with CO_2. Some of the radiation is absorbed, causing parts of the MOF and the trapped gas molecules to transition to higher energy levels. A detector collects radiation that is not absorbed, and our software generates a spectrum of intensity versus frequency.

Traditionally, frequencies are measured in wavenumbers (ν/c) which have units of cm^{-1}. We study the frequencies at which trapped CO_2 absorbs radiation and how they differ from the frequencies at which gas-phase CO_2 absorbs. We look at trends in peak shapes and relative intensities as we change the sample temperature and and as we increase the CO_2 concentration.

1.4   Carbon dioxide

In this thesis we focus on the quantum transitions of the adsorbed carbon dioxide molecule. CO_2 is a linear triatomic molecule composed of a carbon atom double-bonded to two oxygens, one on each side. To describe its motion, we use coordinates that represent the translations of its center of mass, its internal vibrations, and rotations about its principle axes. We can further break up the molecule's vibrations into normal modes. CO_2 gas has three vibrational modes.

1. INTRODUCTION

Because adsorbed CO_2 is subject to the laws of quantum mechanics, it can translate, vibrate, and rotate only with discrete energies. A CO_2 molecule can absorb radiation and transition into an excited state with higher energy; however it can only absorb photons at particular frequencies corresponding to the energy difference between the initial and final states.

In this thesis we are primarily concerned with vibrational transitions of adsorbed CO_2 because they occur in an energy range that matches the mid- to near-infrared energy range of our radiation source. At room temperature, virtually all of the molecules are in their vibrational ground state, so in our spectra we see transitions from the ground state to the first or second vibrationally excited state.

When CO_2 transitions to its first vibrationally excited state, its change in energy corresponds to the frequency of an infrared photon. As we will discuss in Chapter 3, experimentalists can determine the energy spacing between the molecular vibrational levels via measuring these photon frequencies. We call the three frequencies associated with the transitions to the first excited states of CO_2's three vibrational modes ν_1, ν_2, and ν_3. ν_1 corresponds to excitation of the first mode, which is a symmetric stretch, ν_2 corresponds to a transition of the second mode, which is a bending of the molecule, and ν_3 corresponds to excitation of the third mode, which is an asymmetric stretch. In Chapter 2 we will discuss these modes and their transition frequencies in more detail. In gas phase CO_2, these transitions occur at 1388 cm^{-1} (ν_1), 667 cm^{-1} (ν_2), and 2349 cm^{-1} (ν_3) (23).

Rotational and translational transitions of adsorbed CO_2 correspond to microwave frequencies, which are outside of our spectral range. We can, however, see rotational and translational sidebands near our vibrational peaks in our spectra, in which molecules undergo a vibrational and rotational, or a vibrational and translational, transition upon absorbing a photon. We can also see combinations of two or more vibrational transitions. In Chapter 3 will describe how only the transitions of certain modes are infrared active and appear in our spectra.

When a CO_2 molecule is trapped in an enclosure, such as when it is adsorbed to a MOF, its motion is constrained. It cannot translate freely. Furthermore, the CO_2 may not be able to freely rotate. In this case it becomes relevant to consider librational motion of the molecule. A libration can be thought of as a rotational vibration, in which

the molecule is constrained to rotate only over a small angle. Librational energy levels of trapped CO_2 are quantized as well, and we will discuss them further in Chapter 2.

Roughly 99% of naturally abundant carbon dioxide is $^{12}C^{16}O_2$ and 1% is $^{13}C^{16}O_2$. The energy spacings between the levels of these two carbon dioxide isotopologues differ from one another. As we will see in Chapter 2, the difference in spacing leads to a different transition frequency for each isotopologue. Other isotopologues, with ^{18}O substituting one or both of the ^{16}O nuclei, exist as trace percentages of natural CO_2, but their infrared peaks are too small to be visible in our spectra.

1.5 Methane

Geometrically, methane (CH_4) is described as a spherical top. The carbon is located at the center and is covalently bonded to four hydrogens in a tetrahedral orientation. Methane's motion is more difficult to describe than that of CO_2. CH_4 has fifteen degrees of freedom, which we split into three coordinates for translations, three for rotations about the three principle axes, and nine coordinates to describe vibrations. Degeneracy reduces these to four vibrational modes. Of these modes, only two of them are infrared active, and only one of those has energy spacings that correspond to the infrared region we probe. This mode is a triply degenerate asymmetric stretching mode, which occurs at 3019 cm^{-1} (23). Methane has no permanent dipole or quadrupole moment, so it interacts with MOFs via dispersion forces primarily. Thus, it binds to MOF-74 much more weakly than carbon dioxide does.

1. INTRODUCTION

2

Quantum mechanics of motion

2.1 Overview

In describing the motion of the CO_2 molecule, for our purposes we may ignore electronic motion, as the electrons remain in their ground states throughout our experiments. Thus we model the molecule as three nuclei bound together.

A three-particle system typically has nine degrees of freedom. We can describe the motion of the CO_2 molecule by assigning three spacial coordinates to each nucleus. For our purposes, however, it is most convenient to work with a different set of coordinates. We assign three coordinates (x, y, z) to represent the motion of the center of mass of the molecule. We then treat the molecule as a rigid rotor and assign two orientation angles (θ, ϕ) to describe rotations about the molecule's principle axes. The remaining four coordinates represent vibrational motion of the molecule.

As mentioned in § 1.4, carbon dioxide's vibrational and rotational energies are quantized. When it is bound to a metal-organic framework, its translational energies are quantized as well. A CO_2 molecule can transition into an excited state with higher energy via absorption of photons at frequencies corresponding to the energy difference between the molecule's initial and final states. We discuss absorption of radiation further in § 3.1.

We can treat rotations, vibrations, and translations separately because their transitions have dissimilar energies. For CO_2, rotational energy spacings correspond to frequencies on the order of 1 cm^{-1} and vibrational spacings are on in the thousands of cm^{-1} range, where cm^{-1} are the traditional units for infrared frequencies. In gas

phase, the translational energies are not quantized, although when bound to a MOF, CO_2 translational energies become quantized and have spacings on the order of 100 cm^{-1} (11).

2.2 Vibrations

In this work we are primarily concerned with vibrational transitions of adsorbed CO_2. At room temperature, virtually all of the molecules are in their vibrational ground state, so in our spectra we see transitions from the ground state to the first or second vibrationally excited state.

As a first approximation, we treat the CO_2 molecule as a system of coupled oscillators. Classically, we can solve the coupled-oscillator problem of three masses connected by two springs and find the normal vibrational modes of the molecule and its equations of motion. The resulting modes are a symmetric stretch, in which the center of mass remains fixed and the connecting springs expand and contract together; an antisymmetric stretch, in which one spring contracts while the other expands; and two bending modes, which, for a symmetric molecule such as CO_2, are degenerate.

Thus our four remaining coordinates are sufficient to describe the molecular vibrations. We use dimensionless variables (q_1, q_2, q_3) to describe vibrational motion of the CO_2 molecule along the three normal modes. Figure 2.1 shows a schematic of the vibrational modes of CO_2. These normal modes can be modeled as quantum mechanical harmonic oscillators, for which exact solutions to the Schrödinger equation exist.

Plugging the effective potential energy of each mode into the Schrödinger equation, and solving via either the power series method or the ladder operator method, as detailed in Chapter 3 of Griffiths' *Introduction to Quantum Mechanics*, we can find the eigenenergies E_i associated with each vibrational mode (24),

$$E_i = h\nu_i \left(v_i + \frac{1}{2} \right), \tag{2.1}$$

where, v_i is the quantum number of the vibrational mode i, and i takes on the values of 1, 2, and 3, for the symmetric stretching, doubly-degenerate bending, and asymmetric stretching modes, respectively. From Hooke's Law we have

$$\nu_i = \frac{1}{2\pi} \sqrt{\frac{k_i}{m_i}}, \tag{2.2}$$

ν₁: symmetric stretch

ν₂: doubly degenerate bend

ν₃: asymmetric stretch
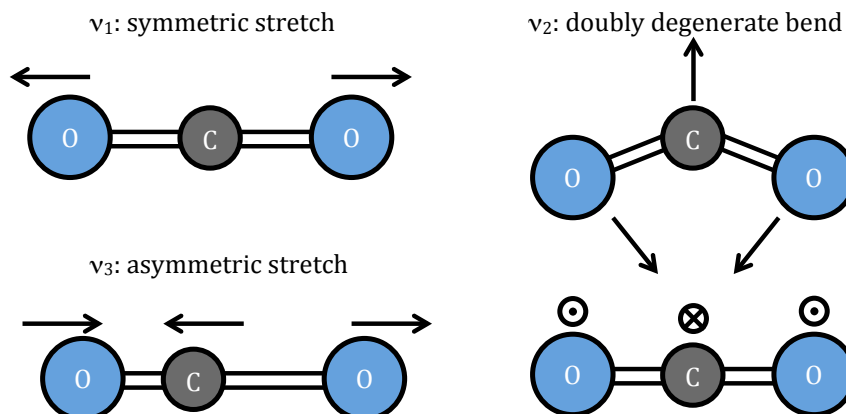
Figure 2.1: The three normal modes of the CO_2 molecule -

where k_i is the effective spring constant and m_i is the effective mass of the oscillator describing the mode i.

The energy spacings between levels are given by

$$\Delta E_i = h\nu_i. \tag{2.3}$$

We can make a more accurate approximation of the vibrational energies of the CO_2 molecule by considering anharmonicity in the vibrations. In general, we can approximate the energy levels of a slightly anharmonic oscillator polyatomic molecule using perturbation theory. However, we can no longer consider the modes separately because the anharmonicity couples them such that they are no longer truly normal modes. Using the notation from Buckingham (25), we express the anharmonic perturbing Hamiltonian $\hat{H}_a$ for a polyatomic molecule as

$$\hat{H}_a = \sum_{i,j,k} V_{ijk} q_i q_j q_k + \sum_{i,j,k,l} V_{ijkl} q_i q_j q_k q_l + ..., \tag{2.4}$$

where V_{ijk} and V_{ijkl} are anharmonic constants specific to the molecule being modeled and the q_i terms represent motion along the normal modes of the harmonic approximation.

Including these anharmonic terms allows us to reach a better approximation for the energy spacings of the CO_2 vibrational levels. The spacings are no longer all the same, as they were in the harmonic approximation. In addition to affecting the energy

spacings such that the energy difference between the first and second levels is slightly different from the energy difference between the second and third levels, anharmonicity also allows for overtone transitions to occur, in which the vibrational quantum number v_i of a particular mode changes by two upon transition.

The energy differences between the vibrational ground state of the CO_2 molecule and each mode's first excited state have been determined experimentally and calculated theoretically (26). When CO_2 transitions to the first excited level of the asymmetric stretch while remaining in the ground levels for the other two modes, the energy change,

$$\Delta E_3 = E_{(0,0,1)} - E_{(0,0,0)}, \tag{2.5}$$

where $E_{(0,0,0)}$ is the total vibrational energy in the ground state and $E_{(0,0,1)}$ is the vibrational energy in the state in which one quantum of the asymmetric stretch mode is excited, is equivalent to the energy of an infrared photon of frequency ν_3. Thus in infrared spectrometry the energy difference ΔE_3 is traditionally expressed as a fundamental transition frequency ν_3.

Experimentally, the fundamental frequencies–ν_1, ν_2, and ν_3–of the three modes of the free CO_2 molecule have been found to be 1388.3, 667.3, and 2349.3, respectively (23).

2.3   Rotations

To describe the rotational motion of the carbon dioxide molecule, we consider CO_2 to be a linear rigid rotor that rotates about two principle axes perpendicular to the nuclear axis with energy

$$\begin{aligned} E_{rotor} &= \frac{\hbar^2 J(J+1)}{2I} \\ &= hcB_e J(J+1) \end{aligned} \tag{2.6}$$

where J is the rotational (angular momentum) quantum number and $B_e = h/(8\pi^2 cI)$ is the rotational constant of CO_2, and I is the molecule's moment of inertia.

In reality the rotational constant B depends on the vibrational state of the molecule, as anharmonicity causes the average bond lengs of the molecule, and hense I to be slightly larger in the excited vibrational states.

For rotations of CO_2 about the two axes perpendicular to its bond axis, the rotational constant $B_e = 0.39 cm^{-1}$ [27]. In gas-phase CO_2, infrared spectra show rotational sidebands in which the molecule undergoes a transition to a different vibrational level and a different rotational level. In fact, as we will discuss in § 2.5, gas phase CO_2 is quantum mechanically forbidden from transitioning to the first excited asymmetric vibrational level alone and must simultaneously transition to a different rotational level.

When a carbon dioxide molecule is bound to a metal-organic framework, it is constrained such that it cannot rotate freely. For adsorbed CO_2, therefore, rotational sidebands do not appear in our spectra. (In § 2.5 we will describe how interaction with the MOF allows for transitions in which only the vibrational quantum number of the CO_2 molecules changes).

2.4 Librations and translations

In the gas phase, carbon dioxide is unbound and can translate at any energy. When bound to a MOF, however, its translations become quantized. Similarly, when bound to a metal-organic framework structure, a CO_2 molecule is unable to rotate, yet it may be able to librate. A libration can be thought of as an angular vibration, in which the molecule is constrained to rotate only over a small angle. A mean libration angle of CO_2 trapped in channels of a crystal framework has been reported at 28^0 [28].

When CO_2 is bound to a MOF, five intermolecular modes are expected. These modes comprise constrained three-dimensional translations of the center of mass and two constrained rotations (librations).

By treating the potential well in which the molecule's center of mass sits as that of a three-dimensional harmonic oscillator, we arrive at approximate translational eigenenergies of

$$E_{trans} = h\nu_1 \left(n_1 + \frac{1}{2} \right) + h\nu_2 \left(n_2 + \frac{1}{2} \right) + h\nu_3 \left(n_3 + \frac{1}{2} \right) \tag{2.7}$$

where n is the translational quantum number, ν_1, ν_2, and ν_3 now represent translational frequencies in each of the three normal directions.

Broad translational bands have been observed in spectra of adsorbed molecular hydrogen in metal organic frameworks, [19, 21], the breadth of which are attributed

to a range of slightly different potentials experienced by molecules bound in different unit cells and to lifetime broadening (21).

Wu et al. report that these intermolecular transitions in CO_2 bound to Mg-MOF-74 lie in the 30-60 cm^{-1} range (29). Dietzel et al. reports a translational transition peak in their infrared spectra of CO_2 in Ni-MOF-74 at ~ 70 cm^{-1}(11). However, we were unable to identify any of the five intermolecular transitions in our infrared spectra, for reasons that we discuss in Chapter 6.

2.5   Selection rules

In gas phase, the overall symmetrization requirement of the wavefunction describing CO_2 prohibits the molecule from undergoing pure rotational transitions in which the change in the angular momentum quantum number ΔJ is odd. Furthermore, the pure fundamental antisymmetric vibrational transitions are prohibited. Here we give a informal theoretical explanation for these selection rules. For a more detailed treatment, see Chapter 4 of Herzberg's *Molecular Spectra and Molecular Structure* Volume 2. (30).

The ^{16}O atoms in $C^{16}O_2$ are identical bosons. Therefore, when the molecule undergoes a rotation and the oxygens are exchanged, the overall wavefunction describing the CO_2 molecule must be unchanged in sign (24).

$$\Psi = \psi_e \psi_v \psi_r \psi_n, \tag{2.8}$$

where ψ_e, ψ_v, ψ_r, and ψ_n represent the electronic, vibrational, rotational, and nuclear components of the overall wavefunction Ψ, respectively.

As mentioned previously in § 2.1, the electronic wavefunction does not change with the molecular transitions we are studying, so we may disregard it in this treatment. Similarly, the wavefunction describing the nuclei of the constituent atoms remains unchanged under exchange of the oxygens (31). Thus we focus on the rovibrational wavefunction Ψ_{rv}

$$\Psi_{rv} = \psi_v \psi_r \tag{2.9}$$

and require that it be symmetric under interchange of the oxygens.

When the oxygens are exchanged, the sign of rotational wavefunction changes according to $(-1)^J$.

When considering vibrations, we will focus on the fundamental asymmetric stretch transition, in which the symmetric and bending modes remain in their ground levels. We find that in the molecule's ground state ($v_1 = v_2 = v_3 = 0$), the vibrational wavefunction keeps the same sign upon exchange of the oxygen nuclei. Thus, in this vibrational state, rotational states with odd values of J do not exist.

On the contrary, when CO_2 is in the first excited state of the asymmetric stretch ($v_1 = v_2 = 0, v_3 = 1$), the vibrational wavefunction ψ_v is antisymmetric under exchange of the oxygen atoms. In this vibrational state, rotational states with even values of J do not exist.

Therefore, when the CO_2 makes a fundamental asymmetric vibrational transition (ν_3), ΔJ cannot be zero. In other words, the pure ν_3 CO_2 transition is quantum-mechanically forbidden. In gas phase spectra, we see an envelope of rotational side-bands at higher and lower frequencies than the pure ν_3 transition, but we see no pure vibrational band in the center at 2349 cm^{-1}. The combination rotation and vibration transitions that lead to the sidebands are called rovibrational transitions. Furthermore, conservation of angular momentum further restricts the allowed transitions so that $\Delta J = \pm 1$

This restriction that upon the fundamental asymmetric vibrational transition $\Delta J \neq 0$ is absolute for free CO_2. However, when CO_2 is bound to a MOF, the wavefunction describing the system can be written to include host framework terms. When a bound CO_2 molecule undergoes a vibrational ν_3 transition, a simultaneous transition can occur in the MOF that balances the sign of the total wavefunction describing the system. These MOF-transitions may be associated with only tiny energies changes, such that they have negligible effects on energy spacings of the transitions.

In the adsorbed phase, J is no longer a good quantum number. A particular CO_2 state could be expressed as a linear combination of J levels, but since the coefficients would span large range of J values, it becomes meaningless to talk about rovibrational selection rules in bound CO_2.

2.6   Fermi resonance

When two different transitions have similar energies, such as the fundamental ν_1 transition and the $2\nu_2$ overtone transition in CO_2, the two modes can become coupled and

lead to an effect called Fermi resonance. A fermi resonance can be thought of as an accidental degeneracy. The Fermi resonance in CO_2 can be thought of as as a splitting of the ν_1 transition into two transitions, one of higher energy and one of lower energy. Realistically, it is more accurate to describe both transitions as linear combinations of the ν_1 and $2\nu_2$ transitions.

2.7 Methane

Methane (CH_4), has a tetrahedral geometry, with the carbon at the center, in which the moments of inertia I_a, I_b, and I_c about the three principle axes are all equal. A molecule with this geometry is termed a spherical top (30). Because it consists of five atoms which, although constrained, can move independently, its motion is more difficult to describe than that of CO_2. CH_4 has fifteen degrees of freedom, which we split into three coordinates for translations, three for rotations about the three principle axes, and nine coordinates to describe vibrations. However, its spherical top symmetry leads to vibrational degeneracies that reduce these nine coordinates or degrees of freedom to just four different vibrational modes ν_1, ν_2, ν_3, and ν_4. Experimentally, the fundamental frequencies associated with the modes are $\nu_1 = 2917$ cm^{-1}, $\nu_2 = 1534$ cm^{-1}, $\nu_3 = 3019$ cm^{-1}, and $\nu_4 = 1306$ cm^{-1} (23). Of these transitions, only the $\nu_3 = 3019$ cm^{-1} transition is both infrared active and has energy spacings that correspond to the infrared region we probe. This mode is a triply degenerate asymmetric stretching. When we study spectra of adsorbed CH_4, we focus on the molecule's ν_3 transition.

Because methane has no permanent dipole or quadrupole moment, it interacts with metal-organic frameworks via dispersion forces primarily. Thus, it binds to MOF-74 much more weakly than carbon dioxide does, and its infrared spectra show weaker bands.

3

Infrared spectroscopy

Infrared spectroscopy involves shining radiation on a sample and measuring the frequencies at which the radiation is absorbed by molecules in the sample. These frequencies correspond to quantum energy transitions in the molecules. The infrared spectrum thus provides information on the energy spacings between quantized vibrational, rotational, and translational states of the molecules being studied. In this chapter we discuss how molecules interact with infrared radiation, we introduce some IR spectrometry terminology, and we discuss how interaction of carbon dioxide with a metal-organic framework affects the frequencies of radiation that the molecule absorbs.

3.1 Absorption of radiation

Using time-dependent perturbation theory, we can approximate the interaction of the electric field of an infrared photon with a molecule and find the transition probability of the molecule absorbing the photon's energy and entering an excited state. When charges interact with a photon, we can write the perturbing Hamiltonian as

$$\hat{H}' = \int \vec{E}_{ph} \sum_i q_i dr_i. \tag{3.1}$$

The electric field $\vec{E}_{ph}$ of a photon can be expressed as

$$\vec{E}_{ph} = \vec{E}_o e^{i(\vec{k}\cdot\vec{r} - \omega t)}, \tag{3.2}$$

where $\vec{E}_o$ is the amplitude of the traveling wave, $\vec{k}$ is the wavevector of the photon with $k = 2\pi/\lambda$ and λ being the photon's wavelength, $\vec{r}$ describes a position in space, ω

is the photon's angular frequency, and t denotes time passed. Focusing on the spacial part of the electric field and looking in the limit that the wavelength of the infrared radiation is much larger than the radius of the molecule, we can approximate the electric field as being constant. The perturbing Hamiltonian is then approximately

$$\hat{H}' \approx \vec{E}_o \sum_i q_i r_i$$
$$\approx \vec{E}_o \mu. \tag{3.3}$$

Such a simplification is called the dipole approximation because the perturbing Hamiltonian is taken to be a constant times the dipole moment μ of the molecule. This is a reasonable approximation for our purposes as the length of a CO_2 molecule is roughly 3 Å and the wavelength of a typical infrared ray is four orders of magnitude larger at ~ 3 microns.

Under the dipole approximation, for a molecule to absorb a photon, it must have a dipole moment. More specifically, it must have a nonzero matrix element of the dipole moment operator $\hat{\mu}$ between the initial and final states (see Griffiths' *Introduction to Quantum Mechanics* § 9.1-9.2 (24) for a derivation). This matrix element represents a change in the dipole moment upon transition from the initial state to the final state. All of the transitions producing spectral bands analyzed in this thesis have nonzero dipole moment matrix elements and are thus infrared-active. As is shown in Griffiths (24), the probability of a molecule interacting with the electric field of an infrared photon and undergoing a transition from a state $|\psi_a\rangle$ to another state $|\psi_b\rangle$, to first order, is proportional to

$$P_{a \to b} \propto \frac{|\langle \psi_a | \hat{\mu} | \psi_b \rangle|^2}{(\omega_0 - \omega)^2}, \tag{3.4}$$

where ω is the frequency of the incident radiation and $\hbar\omega_0$ is the energy difference between the initial and final states. As conservation of energy requires, this probability is virtually zero unless $\omega \approx \omega_0$.

Thus a particular transition in a molecule will correspond to a narrow range of infrared frequencies that produce an absorption band in an infrared spectrum. The maximum of the band, which has frequency proportional to the energy difference between $|\psi_a\rangle$ and $|\psi_b\rangle$, is traditionally termed the peak of the band. Absorption bands due

to pure vibrational transitions are termed Q-transitions, whereas rotational sidebands, which are combination vibrational and rotational transitions, are denoted by other letters, depending on by how many units the rotational quantum number changes. A Q(0)-transition refers to a molecule remaining in its ground rotational state while undergoing a purely vibrational transition. Q(1) denotes a Q-transition in which the molecule remains in its first rotationally excited state.

In CO_2, the fundamental Q(0)-transition of the asymmetric-stretch (ν_3) mode, that is, the transition from the ground vibrational state to the first asymmetrically-vibrational excited state, is infrared-active, as it corresponds to a dipole moment change. The fundamental symmetric stretch transition ν_1 does not correspond to a dipole moment change and is thus infrared-inactive. However, it is plausible that bound CO_2 could nonetheless produce a symmetric-stretch band, as the MOF may perturb the molecule enough to break the symmetry of that mode and produce a small transition dipole moment, allowing for ν_1 transitions to occur. However, as we will discuss in Chapter 6, such band were not visible in our spectra.

As mentioned in § 2.2, anharmonicity in CO_2 vibrations allows for transitions from the ground vibrational level of a particular mode to its second excited level. These transitions are called overtones.

3.2 Interaction frequency shift

The following analysis relies heavily on the Buckingham's work on solvent effects in vibrational spectroscopy (25). In his seminal paper he employs perturbation theory to approximate the energy levels of diatomic and polyatomic molecules interacting with solvents as a function of the interaction potential energy, U, and its derivatives with respect to the normal coordinates of vibration.

As discussed in § 2.2, the vibrations of a polyatomic molecule can be approximated as a system of harmonic oscillators with each oscillator corresponding to a normal mode. A better approximation for vibrational motion involves incorporating anharmonicity into the vibrational potential-energy terms. Using perturbation theory we can approximate the energy eigenvalues of each vibrational mode. We treat the anharmonic Hamiltonian $\hat{H}'_a$ as a perturbation to the harmonic Hamiltonian $\hat{H}_o$, for which exact solutions exist. When a polyatomic molecule interacts with a solvent, such as

when it is adsorbed to a metal-organic framework, its vibrational energy levels are perturbed further by the interaction between the molecule and the framework. We thus express a new perturbing Hamiltonian $\hat{H}'$ in terms of the interaction potential energy U:

$$\hat{H}' = \hat{H}'_a + U(q_1, q_2, ..., q_n; \tau) - U_e, \tag{3.5}$$

where q_i are the normal coordinates of vibration of the free molecule, τ represents all the positions and orientations of the atoms composing the solvent environment surrounding the molecule. τ depends on the molecule's center of mass and orientation relative to the solvent molecules, and U_e is the interaction potential energy in the molecule's equilibrium position. U_e is an expression of the binding energy of adsorption.

After expanding U as a Taylor series about the equilibrium position of the molecule with respect to vibrations, that is at $q_1 = q_2 = ... = q_n = 0$, Buckingham performs first and second order perturbation theory to find the energy eigenvalues of the adsorbed molecule:

$$
\begin{aligned}
W_{v_1, v_2, ..., v_i, ...}(\tau) &= W_v(\tau) \tag{3.6} \\
&= W_v^{(0)} + U_e - \sum_i \beta_i \frac{(U_i')^2}{hc\nu_i} + \sum_i (v_i + \frac{1}{2})\beta_i[U_{ii}'' - 12\sum_j \frac{\beta_j}{hc\nu_j}U_j'V_{iij}] + ...,
\end{aligned}
$$

where W_v is the energy of a particular vibrational state of the molecule interacting with solvent, $W_v^{(0)}$ is the energy of the corresponding state in the isolated molecule, the v_i terms represent energy quantum numbers of the vibrational modes i, $\beta_i = h/(8\pi^2 c\nu_i)$, $U_i' = (\partial U/\partial q_i)_e$ is the partial derivative of the interaction potential energy with respect to the normal coordinate q_i evaluated at the equilibrium position of that mode in the unperturbed molecule, i.e., at $q_i = 0$. At this stage U_i' is still a function of τ. We use the convention that ν_i represents the harmonic oscillator frequency in wavenumbers, which the traditional measure of infrared radiation frequencies and is the reciprocal of wavelength.

The fundamental frequency ν_i, that is, the frequency of the adsorbed molecule's transition to the first excited level of vibrational mode i while remaining at the ground levels for all other modes is given by:

$$
\begin{aligned}
\nu_i(\tau) &= \left[W_{0,0,\ldots,1,0,\ldots}(\tau) - W_0(\tau) \right]/hc \\
&= \nu_i^{(0)} + \frac{\beta_i}{hc} \left\{ U_{ii}'' - 12 \sum_j \frac{\beta_j}{hc\nu_j} U_j' V_{iij} \right\} + ...,
\end{aligned}
\tag{3.7}
$$

where the V_{iij} terms are anharmonic constants for the CO_2, which have been calculated theoretically and can be found in a paper by Suzuki (26).

The observed absorption frequencies $\bar{\nu}_i = \langle \nu_i(\tau) \rangle_0$ are calculated by taking an average of $\nu_i(\tau)$ over all τ, that is, an average over all the discrete orientational and center-of-mass-translational quantum states.

The frequency shift, $\Delta\nu_i = \bar{\nu}_i - \nu_i^{(0)}$, of the observed band upon the molecule's interaction with a solvent is thus

$$
\Delta\nu_i = \frac{\beta_i}{hc} \left\{ \langle U_{ii}'' \rangle_0 - 12 \sum_j \frac{\beta_j}{hc\nu_j} \langle U_j' \rangle_0 V_{iij} \right\} + ...
\tag{3.8}
$$

where $\langle U_i' \rangle_0$ and $\langle U_i'' \rangle_0$ are the average values for all τ of U_i' and U_i'' in the ground vibrational state. For a linear, triatomic, symmetric molecule such as carbon dioxide, the expression in 3.8 becomes simplified. In CO_2 the subscripts i take on the values 1, 2, and 3, where, as before, 1 represents the symmetric stretching mode, 2 the doubly-degenerate bend, and 3 the asymmetric stretch. Symmetry requires that $\langle U_2' \rangle_0 = \langle U_3' \rangle_0 = 0$, which results in approximate frequency shifts of

$$
\begin{aligned}
\Delta\nu_1 &= \frac{1}{8\pi^2 c^2 \nu_1} \left\{ \langle U_{11}'' \rangle_0 - \frac{3}{2\pi^2 c^2 \nu_1^2} \langle U_1' \rangle_0 V_{111} \right\}, \\
\Delta\nu_2 &= \frac{1}{8\pi^2 c^2 \nu_2} \left\{ \langle U_{22}'' \rangle_0 - \frac{3}{2\pi^2 c^2 \nu_2^2} \langle U_1' \rangle_0 V_{221} \right\}, \\
\Delta\nu_3 &= \frac{1}{8\pi^2 c^2 \nu_3} \left\{ \langle U_{33}'' \rangle_0 - \frac{3}{2\pi^2 c^2 \nu_3^2} \langle U_1' \rangle_0 V_{331} \right\}.
\end{aligned}
\tag{3.9}
$$

From here we will focus on $\Delta\nu_3$ and discuss its sign qualitatively. We see that the U_1' influences the frequency shift of the asymmetric stretch transition through the anharmonic constant V_{311}, which was calculated by Suzuki and found to have a negative sign (26).

3. INFRARED SPECTROSCOPY

We can assume that $\langle U''_{33} \rangle_0$ is small compared to $3/(2\pi^2 c^2 \nu_3^2)\langle U'_1 \rangle_0 V_{331}$ and can be ignored (32). This allows us to place the dependence of the frequency shift on the sign of $\langle U'_1 \rangle_0$. If $\langle U'_1 \rangle_0$ is positive, $\Delta\nu_3$ is likely to be positive; the solvent interaction causes a blueshift. If $\langle U'_1 \rangle_0$ is negative, there will likely be a redshift.

If the interaction potential energy increases as the molecule expands via the symmetric stretch and decreases as it contracts, then $\langle U'_1 \rangle_0$ will be positive in that region. We can think of $-\langle U'_1 \rangle_0$ as a measure of the force on the CO_2 molecule due to the interaction with the solvent as it expands or contracts. A positive value of $\langle U'_1 \rangle_0$ is in simpler terms a repulsive force on the CO_2 from the solvent.

To be clear, this repulsion does not push the molecule away from the solvent but rather causes it to contract, as $\langle U'_1 \rangle_0$ is a function of the symmetric vibrational mode, not of translations.

The cause for such a repulsive force remains to be discussed. There has been speculation on the particular conditions likely to result in a blueshift for CO_2 interacting with a metal ion, as occurs when CO_2 is adsorbed to MOF-74: Gregoire et al. claim that a blueshift is more likely to result from an end-on-configuration (33), in which the CO_2 molecule interacts with the solvent mainly via one of its oxygens, such that symmetric and antisymmetric vibrations bring the oxygen closer to the solvent. As we will discuss further in Chapter 4, CO_2 binds to MOF-74 surfaces in such a configuration (29), making a blueshift in ν_3 a reasonable possibility.

To summarize, the asymmetric-stretch fundamental frequency of CO_2 interacting with a solvent may blueshift if the net force on the molecule from the solvent pushes it into a slightly contracted configuration compared to its length in gas phase. If instead the solvent forces the molecule to expand slightly with respect to its gas-phase length, the ν_3 frequency shift is more likely to be to the red.

4

Mg-MOF-74 and the isostructural series

In this chapter we examine Mg-MOF-74 and other members of the MOF-74 isostructural series. We detail the synthesis, structure, and gas adsorption properties of the different MOF-74 species, and we provide a justification for the comparatively high CO_2 affinity of the magnesium compound.

Metal-organic frameworks (MOFs) are characterized by highly porous structures consisting of metal-oxide clusters joined by organic linkers usually containing aromatic rings. They exhibit high surface areas and high affinity for binding gases to their surfaces. In recent years there have been a number of review articles published on MOFs and their gas adsorption capacities (6, 9, 34).

MOF-74 is a particularly interesting metal-organic framework for study because it contains unsaturated coordination metal sites where adsorbates can interact strongly. The structure of the framework surrounding these open metal sites will be described further in § 4.2. MOF-74 has been shown to have a particularly high initial gas uptake compared to other metal-organic frameworks(11). The high gas-affinity of this compound at low-equilibrium-pressure can be attributed to strong interactions between the adsorbate and the metal ion. Characterizing this interaction is important, as MOFs fabricated in the future are likely to contain these highly adsorptive exposed metal sites.

MOF-74 was first synthesized in 2005 by Rosi et al. with zinc as the coordinating metal ion (9). Other names for the compound include M_2(dhtp), M/DOBDC, and

CPO-74-M where M denotes the coordination metal (16, 17, 35).

Hydrogen-storage properties of the MOF-74 isostructural series have been studied, first by Zhou et al., in compounds synthesized with magnesium, manganese, cobalt, nickel, and zinc. FitzGerald et al. expanded on the work, reporting absorption spectra for H_2 in the same five members of the series (36).

The CO_2-adsorption behavior in the MOF-74 series has been characterized more recently by Caskey et al. (35) and other groups, and CH_4-adsorption properties in M-MOF-74 for M=Mg, Mn, Co, Ni, and Zn have been measured by Wu et al. (22) In this chapter we report binding energies of CO_2 in M-MOF-74 for M=Mg, Co, and Ni as well as CH_4 binding energies in all five members of the series.

4.1   Synthesis

The MOF-74 species studied were synthesized by Dr. Jesse Rowsell of the Oberlin Chemistry and Biochemistry Department using a solvothermal process described in Michael Friedman's Oberlin Honors thesis (21) and modified from literature procedures (35). Either water or methanol was used as the activation solvent, and the samples were heated to 200-250°C in flowing nitrogen to drive off solvent molecules, activating the gas-binding sites.

Each MOF sample must be heated above a particular temperature to drive off the solvent, yet not above a temperature at which the structure decomposes. Thermogravimetric analysis (TGA) is used to determine the temperature range for each MOF species for which the solvent has been driven off yet the structure remains intact. Figure 4.1 shows the TGA traces of the samples of Ni-MOF-74 each prepared under different conditions by Dr. Jesse Rowsell of the Oberlin College Department of Chemistry and Biochemistry. The sample heated to 200°C overnight lost mass due to framework decomposition at a lower temperature (320°C) than samples that did not receive this additional preparation, which degraded at 340°C. TGA gives rough boundaries on the temperature range to which the sample can be safely heated, although the framework may be destroyed below the temperature at which mass loss occurs.

Activated MOF-74 is extremely air-sensitive and must be stored in inert gas. Our samples were stored in an argon-filled glove box. MOF-74 contaminated with air
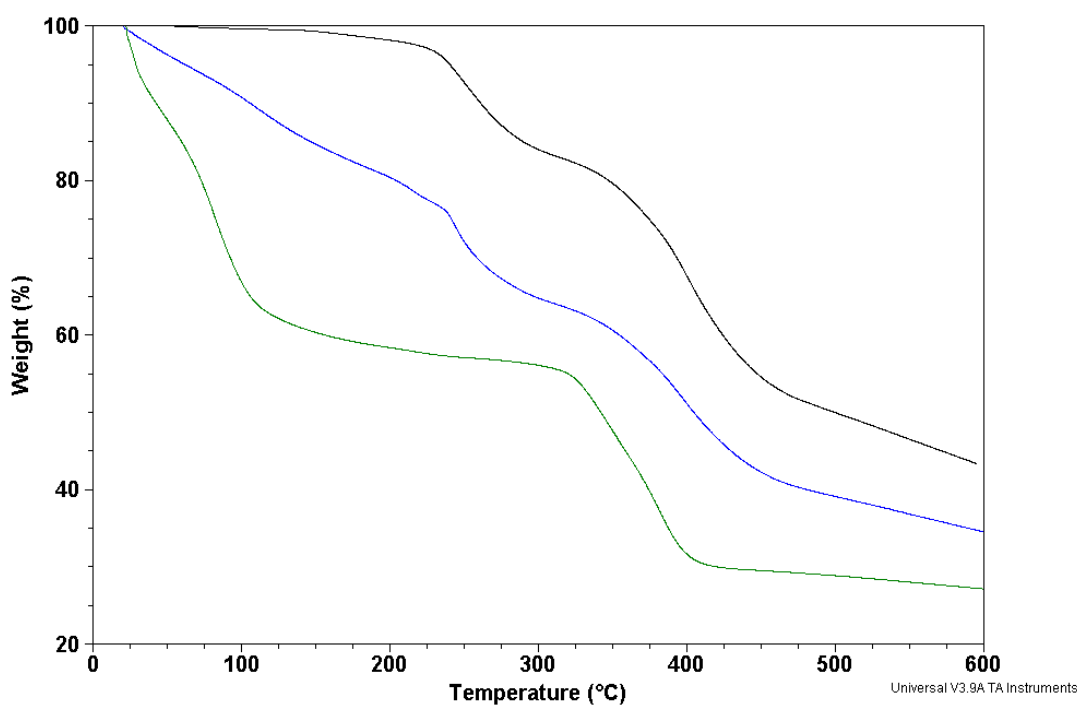
Figure 4.1: Thermogravimetric analysis of three Ni-MOF-74 samples - All three samples were kept under methanol for ∼7d. The green trace represents a sample that was washed with H_2O several times over three days, the black trace represents a sample that was heated to 200^oC overnight, and the blue trace represents a sample with no additional preparation. Sample preparation and TGA were conducted by Dr. J. Rowsell. Mass loss from framework decomposition begins at 340^oC in the green and blue traces and at 320^oC in the black trace, although the framework may be destroyed at lower temperatures, before mass loss occurs.

molecules or with remaining solvent may adsorb less of the desired gas as the contaminating molecules may both fill the adsorbate binding sites and block framework pores, preventing adsorbate from reaching regions of the sample.

4.2 Structure

M-MOF-74 has chemical formula $M_2(C_8H_2O_8)$ (14) where M represents the coordination metal. The framework assumes a honeycomb structure with parallel hexagonal channels, which result from helical M-O-C rods composed of $[O_2M_2](CO_2)_2$, termed secondary building units (SBUs), and are connected to one another by the hydroxy groups of 2-5-dihydroxyterephthalate (dhtp), as is shown in Figure 4.2. The 6-coordinated M^{2+} center is thus bound to five oxygens: three from carboxyl groups and two from hydroxy groups that each connect to the benzene ring of a dhtp. The remaining coordination site is bound to a solvent molecule, which is removed upon activation of the material, allowing adsorbates to bind. The crystal structure is trigonal and belongs to space group R$\bar{3}$ (17). The pores are large enough for gas molecules to access and they allow for significant gas adsorption.
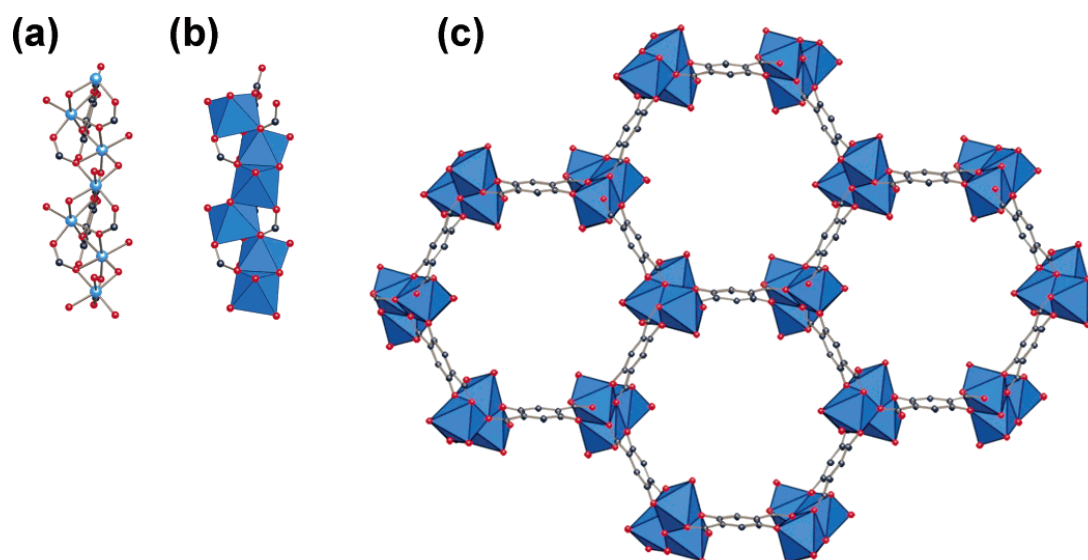

Figure 4.2: MOF-74 structure with secondary building units in blue - Image courtesy of Rosi et al. (9)

Mg-MOF-74 has an estimated surface area of 1495 m^2/g (35), which allows for

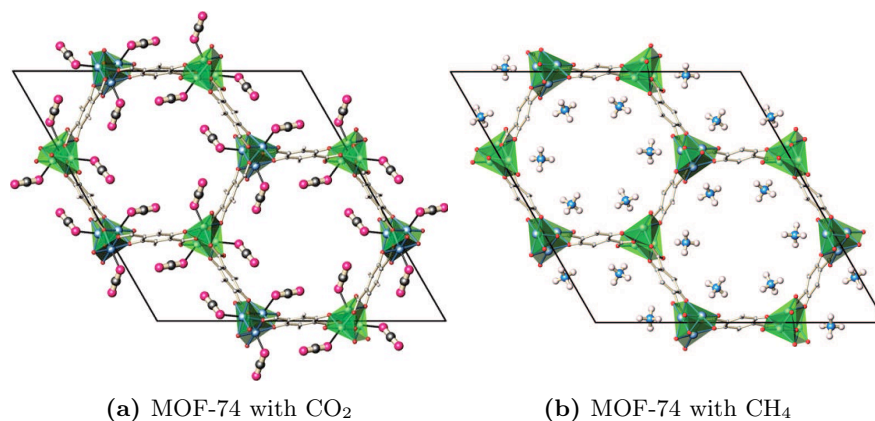**(a)** MOF-74 with CO_2 **(b)** MOF-74 with CH_4

Figure 4.3: Image of MOF-74 with bound CO_2 and CH_4 in their primary sites, from neutron diffraction experiments

significant gas-adsorption per weight. Other members of the series have lower surface areas per mass, which can be attributed in part to their higher formula unit mass, as they contain heavier metals. Estimated surface areas are 1080 m^2/g (35), 1070 m^2/g (13), and 816 m^2/g (34) for Co, Ni, and Zn compounds, respectively.

The MOF-74 samples used in our experiments are in granular crystalline powder form, which is well suited to our particular infrared spectroscopy technique, as will be described further in Chapter 5. Powder X-ray diffraction (PXRD) scans match literature results for the five members of the isostructural series (17), which confirms their crystal structure. Figure (number) shows our scans compared side-by-side with scans published by Zhou et al. (17)

4.3   Gas-adsorption properties

Neutron diffraction experiments conducted by Wu et al. for CO_2 in Mg-MOF-74 indicate that the primary binding site for CO_2 is next to the Mg^{2+} coordination ion (29). Similar neutron experiments for CH_4 in the MOF-74 isostructural series show that CH_4 occupies the same primary binding site (22). Figure 4.3a shows a MOF-74 pore filled with CO_2 occupying the primary sites and Fig. 4.3b shows a pore filled with CH_4 in its primary sites.

Caskey et al. report an initial isosteric heat of adsorption (Qst), which is a measure of binding energy, of 47 kJ/mol for CO_2 in Mg-MOF-74, and they report 41 and 37

4. MG-MOF-74 AND THE ISOSTRUCTURAL SERIES

kJ/mol for CO_2 in Co-MOF-74 and Ni-MOF-74, respectively (35). There exists a range of published values for Qst in Mg-MOF-74, ranging from 39 to 73 kJ/mol (11, 35, 37, 38). The variation may be due to large errors in the measurement techniques or to differences in quality of the samples investigated.

The initial Qst values for CH_4 and CO_2 in the isostructural series are given in Table 4.1 (22, 35). Clearly, MOF-74 has a significantly higher CO_2 affinity than CH_4 affinity.

Table 4.1: Isosteric heats of CH_4 and CO_2 in MOF-74 CH_4 values are from (22); CO_2 values are from (35).

MOF compound	CH_4 initial Qst (kJ/mol)*	CO_2 initial Qst (kJ/mol)
Mg-MOF-74	18.5	47
Mn-MOF-74	19.1	-
Co-MOF-74	19.6	41
Ni-MOF-74	20.2	37
Zn-MOF-74	18.3	-

Fig. 4.4 shows adsorption isotherms of CO_2 in Mg-, Co-, and Zn-MOF-74 conducted at room temperature. The curves match data published by Caskey et al. (35), except that our Zn-MOF-74 sample shows an even higher uptake than that in (35). That our isotherms yield as high or higher CO_2 uptakes and that the shapes of our isotherm curves match those from the literature indicate that the materials used in our infrared spectroscopy measurements are relatively pure and uncontaminated.

Practically, isotherm measurements require a much larger volume of powder sample than infrared spectroscopic measurements require. Thus we did not conduct a Mn-MOF-74 CO_2 isotherm for lack of a sufficient quantity of sample.

Clearly, Mg-MOF-74 has a higher uptake of CO_2 than the other members of the series, even at atmospheric pressure. In Mg-MOF-74, the Mg-O bonds in the framework have high ionic character compared to those of other M-MOF-74 species (35), which we attribute to the comparatively small ionic radius of magnesium. We speculate that more polar bond results in a stronger electric field that the CO_2 molecule feels, causing the CO_2 to interact more strongly at the metal site in Mg-MOF-74 than in the other series members.
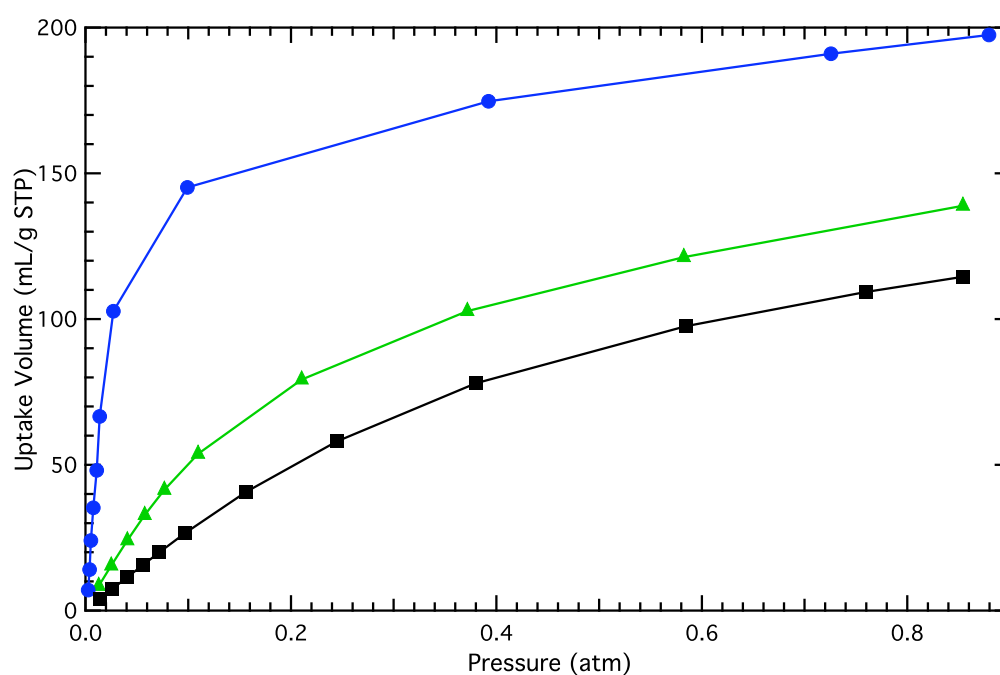
Figure 4.4: Adsorption isotherms of CO_2 in three MOF-74 species - The circles, triangles, and squares represent Mg-, Co-, and Zn-MOF-74 isotherms, respectively. Lines are drawn between points to aid in viewing. The curves match isotherm data published by Caskey et al. (35).

Because CH_4 lacks permanent dipole and quadrupole moments it interacts with the MOF primarily via dispersion forces rather than electrostatic forces. Thus the increased electric field in the magnesium compound leads to only a minor increase CH_4-affinity. Thus, other factors dominate and Ni-MOF-74 is reported to have the highest CH_4-affinity of the members of the series (22).

5

Experimental apparatus and procedure

This chapter contains an overview of the experimental setup for conducting variable temperature, Fourier transform infrared spectroscopy. The spectrometer consists of a modified Bomem DA3 Michelson interferometer with a globar infrared source and either a calcium fluoride (CaF_2) or a potassium bromide (KBr) beam splitter. The spectrometer contains two sample compartments, one of which is used for taking room-temperature spectra, and the other of which is equipped with a custom-made vacuum chamber and cryostat for low temperature-experiments. A mercury cadmium telluride (MCT) detector, cooled with liquid nitrogen, collects infrared signal, and Bomem software performs the Fourier transform to produce infrared spectra, which are saved to a computer.

5.1 The Michelson interferometer

Fourier transform infrared spectroscopy (FTIR) relies on the use of a Michelson interferometer to create a time-varying source of infrared radiation. The time-domain interferogram is converted via a Fourier transform to the frequency-domain, such that the degree to which each frequency is absorbed by the sample can be measured, up to a specified resolution.

In our spectrometer, a polychromatic infrared beam is split, sent down two paths, one to a fixed mirror and one to a movable mirror, and then recombined to create

a time-varying interference pattern. For a particular wavelength λ, fully constructive interference occurs when the path difference between the two beams, Δx, is equal to $m\lambda$ for integer values of m, and fully destructive interference occurs when $\Delta x = (m + \frac{1}{2})\lambda$.

Output from the detector shows intensity as a function of time. Time is related to Δx using the mirror speed, and an interferogram of intensity versus path difference is produced. When $\Delta x = 0$, the beams are at zero path difference (ZPD), and all wavelengths interfere constructively, producing a sharp peak in the interferogram. For nonzero values of Δx, different wavelengths combine constructively and destructively. The Bomem software performs a Fourier transform on the interferogram, producing a spectrum of intensity versus frequency.

In our spectrometer, an HeNe laser with a precisely known wavelength determines the distance traveled by the mirror. A white light source is used to determine the location of ZPD so that all scans of the mirror through a complete cycle have same starting point.

The frequency-resolution of the spectrum depends on the distance covered by the movable mirror. The resolution, measured in cm^{-1}, is the reciprocal of the maximum distance traveled by the mirror. The maximum resolution achievable with this apparatus is 0.04 cm^{-1}. High-resolution spectra are more susceptible to noise and to drift in sample and spectrometer conditions than low-resolution spectra are, because they take longer to obtain. Unless otherwise noted, all spectra in this thesis were taken at 1 cm^{-1} resolution.

5.2 DRIFTS

The typical infrared spectroscopic method used to probe interactions between an adsorbate and a host is transmission spectroscopy, in which infrared radiation passes through the sample and is detected. Absorption signal manifests as dips in detected intensity at particular frequencies.

As granular powders, MOFs scatter too much incident radiation for this method to be effective. If a thin film of MOF sample were fabricated, such that scattering would be minimal, the path length of radiation in the sample would be so small that the absorption signal from CH_4 and other molecules with only small induced dipoles would be too weak to analyze.

Therefore, we use a method called diffuse reflectance infrared Fourier transform spectroscopy (DRIFTS), which takes advantage of the high level of scattering from the powder MOF to increase the path length through which infrared radiation interacts with the sample, thus enhancing the absorption signal.

MOF samples in forms other than powder can be prepared but preparation is much more difficult than for powders. Pressing pure-MOF pellets is very difficult; thus MOF powders are diluted with KBr powder before pressing. Single-crystal MOFs in existence are too small for IR spectroscopy, and free-standing thin films cannot be made. Air-sensitivity of the materials complicates the sample preparation process, making it most practical to produce MOF samples in powder form. Thus DRIFTS is a practical IR spectroscopy method for MOFs.
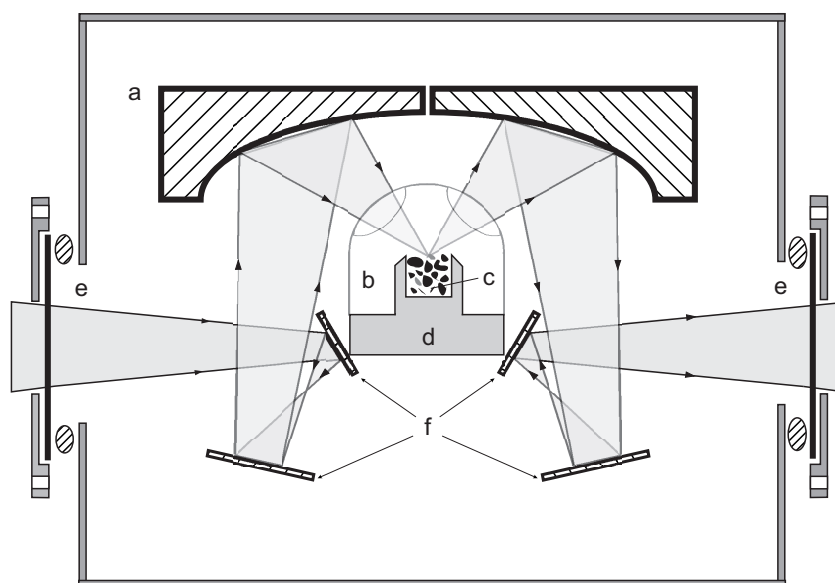
Figure 5.1: Schematic of radiation propagation through DRIFTS optics within a sample compartment (39) - Symbols: (a) ellipsoidal mirrors, (b) high-pressure dome, (c) sample, (d) copper sample holder, (e) CaF_2 windows, (f) mirrors (image courtesy of Y. E. Strangas).

Figure 5.1 shows a schematic of the DRIFTS optics. Radiation enters the chamber and is focused onto the sample by a series of mirrors. It scatters multiple times off of the irregularly shaped powder grains, which results in a long path length in which the radiation interacts with the sample and an increased probability of absorption.

Radiation that is not absorbed is reemitted at a random angle, then reflected and focused by an ellipsoid mirror, and sent into the detector.

This setup is ideal for probing weakly infrared active adsorbates. DRIFTS is less ideal for systems that have high infrared activity. For example, because the antisymmetric stretch mode of adsorbed carbon-dioxide is strongly active in the infrared, our DRIFTS method can lead to signal saturation at high concentrations of adsorbed CO_2, in which all of the radiation at that frequency is absorbed. In the event of CO_2 signal saturation, we study the absorption peak due to $^{13}C^{16}O_2$, a naturally occurring isotopologue of $^{12}C^{16}O_2$, which occupies 1% of the carbon dioxide in our system and thus produces a smaller adsorbed-phase signal than $^{12}C^{16}O_2$.

5.3   The sample compartments

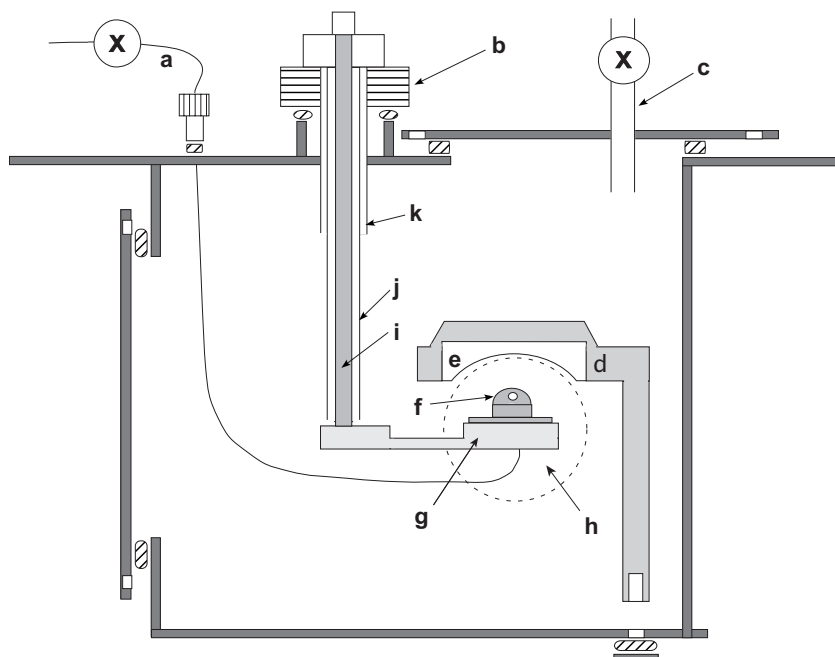**Figure 5.2: Schematic of liquid helium cryostat used in variable temperature DRIFTS** - Symbols: (a) gas line, (b) vertical alignment stage, (c) vacuum line, (d) DRIFTS optical mount, (e) ellipsoidal mirror, (f) high-pressure sapphire dome, (g) copper sample holder, (h) CaF_2 window, (i) copper cold finger, (j) radiation shield, and (k) cryostat vacuum shell, (image courtesy of Y. E. Strangas).

The two sample compartments are equipped with DRIFTs optics and a sample mount. The right compartment contains a cryostat for cooling the sample with liquid nitrogen or liquid helium. Figure 5.2 shows a schematic. The sample is enclosed in a dome with sapphire windows, transparent between 1600 and 15000 cm-1, and is sealed with an indium o-ring, which unlike rubber o-rings maintains its seal down to our base temperature of 10K and below. Surrounding the sample mount is a vacuum chamber with a CaF_2 windows through which radiation enters, travels through the DRIFTS optics, and exits. Cooling occurs via a modified Janis Research Company ST-300T cold finger that transports liquid cryogens. At the base of the cold-finger is a heating element with a maximum temperature of 200 ^{o}C. A Model 331 Lakeshore cryogenic temperature controller with DT-670 silicon diode cryogenic temperature sensors sets and measures the sample temperature. We regulate the systems temperature by setting to the first sensor, which is situated at the base of the cold finger, next to the heating element. The other sensor is placed directly beside the sample dome and gives a more accurate reading of the sample temperature. Further description of the cryogenic apparatus and low-temperature procedure can be found in a paper by FitzGerald et al. (40).

The left sample compartment is configured for room-temperature experiments. Figure 5.3 a photograph of the room-temperature apparatus. The sample fills a recess cup, which is screwed into a removable copper stand. A zinc selenide (ZnSe) dome, sealed to the copper stand with a rubber o-ring, encloses the sample and allows pressures over 100 bar to be applied. The stand is screwed to an aluminum bracket, which holds the sample in place within the DRIFTS optics in the sample compartment.

5.4   Concentration measurement

Adsorbates are let into the sample via a gas line. The number of moles of gas introduced to the sample is calculated using the Ideal Gas Law, with knowledge of the volume and pressure of the gas introduced. Volumes were measured using a calibrated volume of 25 cm^3. The volume of the tubes into which gas is loaded before opening a valve to the sample-volume is 9.90 cm^3. The room-temperature compartment has a measured sample-volume of 4.92 cm^3 and the low temperature compartment has a sample-volume of 1.92 cm^3. By measuring the equilibrium pressures before and after opening to the
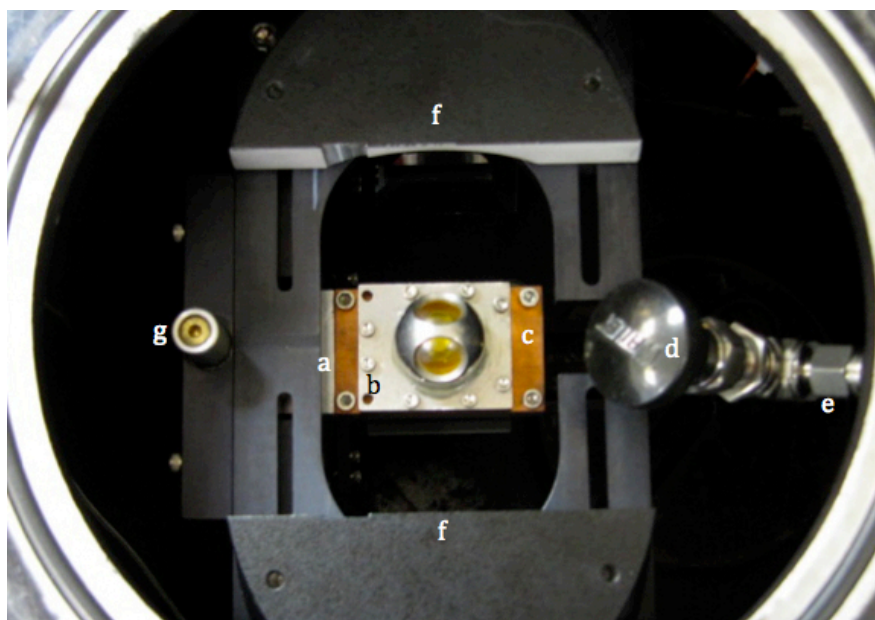
Figure 5.3: Photograph of room-temperature sample holder and compartment in spectrometer - Symbols: (a) aluminum sample bracket, (b) High pressure ZnSe dome, (c) copper sample holder, (d) gas valve, (e) high-pressure gas line, (f) ellipsoid mirrors, and (g) vertical alignment adjust.

sample and comparing the final pressure to the expected equilibrium pressure if no adsorption were to occur, we calculate the number of moles of gas adsorbed. By measuring the mass of MOF sample in the system before loading it, we determine the number of gas molecules adsorbed per sample formula unit. We call this method for determining concentration of adsorbed gas the isotherm method.

5.5 Data collection and manipulation

Each spectrum taken is an average of multiple scans. By averaging 50 or 100 scans, we reduce random noise in our spectra.

Raw spectra of the MOF sample with adsorbate are referenced to pure-MOF spectra to obtain absorbance spectra showing peaks due to adsorbate molecules. If a reference spectrum has intensity $I_o(\omega)$ and a spectrum with adsorbate has intensity $I(\omega)$, an absorbance spectrum showing absorbance $A(\omega)$ is found by calculating

$$A(\omega) = -\log \frac{I(\omega)}{I_o(\omega)}. \tag{5.1}$$

In general we are more interested in relative absorbance than absolute absorbance because a variety of factors that change from experiment to experiment affect the measured absorbance magnitude, such as the quantity of sample and the optical alignment.

In principle, absorbance spectra show only peaks due to adsorbate molecules. In practice, interactions between the adsorbate and the host can cause shifts in the host peaks, leading to differential peaks in the absorbance spectrum where a shifted host peak is divided by the reference host peak. Differential peaks are easily recognizable and can be disregarded. We apply a piecewise linear baseline correction and a fourfold interpolation to each absorbance file.

Carbon dioxide and methane are infrared-active in the gas phase as well as the adsorbed phase; thus gas-phase peaks appear in our CO_2 and CH_4 spectra. In general gas peaks are significantly sharper than adsorbed features making it straightforward in practice to distinguish one from the other. Nonetheless, spectra displayed in this thesis at pressures above 100 mbar have gas phase signal removed through the following procedure: Raw spectra are taken of CO_2 or CH_4 in a sample of CaF_2, which adsorbs no gas and scatters infrared radiation. Spectra of CaF_2 with gas-phase CO_2 or CH_4

are referenced to spectra of CaF_2 at vacuum to create absorbances showing only gas-phase peaks. These spectra are subtracted from absorbances of CO_2 or CH_4 in the MOF host at comparable equilibrium pressures to create absorbance spectra that in principle show adsorbed-phase peaks alone. In practice, some gas phase peaks remain after subtraction, but they are easily recognized and ignored.

6

Results and analysis

In this chapter we present and analyze spectroscopic data of carbon dioxide adsorbed to Mg-MOF-74. We compare spectra of CO_2 in Mg-MOF-74 to spectra of CO_2 in Mn-, Co-, and Zn-MOF-74 and discuss relative peak shifts among the species. Finally, we present spectra of methane adsorbed to Mg-MOF-74 and comment on differences in adsorption capacity for CH_4 versus CO_2.

6.1   Overview

Figure 6.1 displays two absorbance spectra of CO_2 bound to Mg-MOF-74 at concentrations of 0.21 and 0.50 CO_2 per open Mg site. For MOF-74 we typically measure concentration in adsorbed molecules per open metal site, which is equivalent to adsorbed molecules per half formula unit and is what Liu et al. used in their neutron diffraction investigations (15). Our estimate for the equilibrium time at room temperature is on the order of three minutes, although this estimate is based on memory and should be rechecked.

There are two principle regions of the spectra in which peaks appear. A lower frequency region (2200-2500 cm^{-1}) has bands that we associate with the adsorbed-phase ν_3 transition of CO_2. A higher frequency region (3500-3800 cm^{-1}) contains bands due to adsorbed-phase combination-mode transitions consisting of the the fundamental symmetric stretch transition plus the fundamental asymmetric stretch transition ($\nu_1 + \nu_3$) and the overtone of bending mode transition plus the fundamental asymmetric stretch ($2\nu_2 + \nu_3$). The two combination-mode transitions are altered by the Fermi
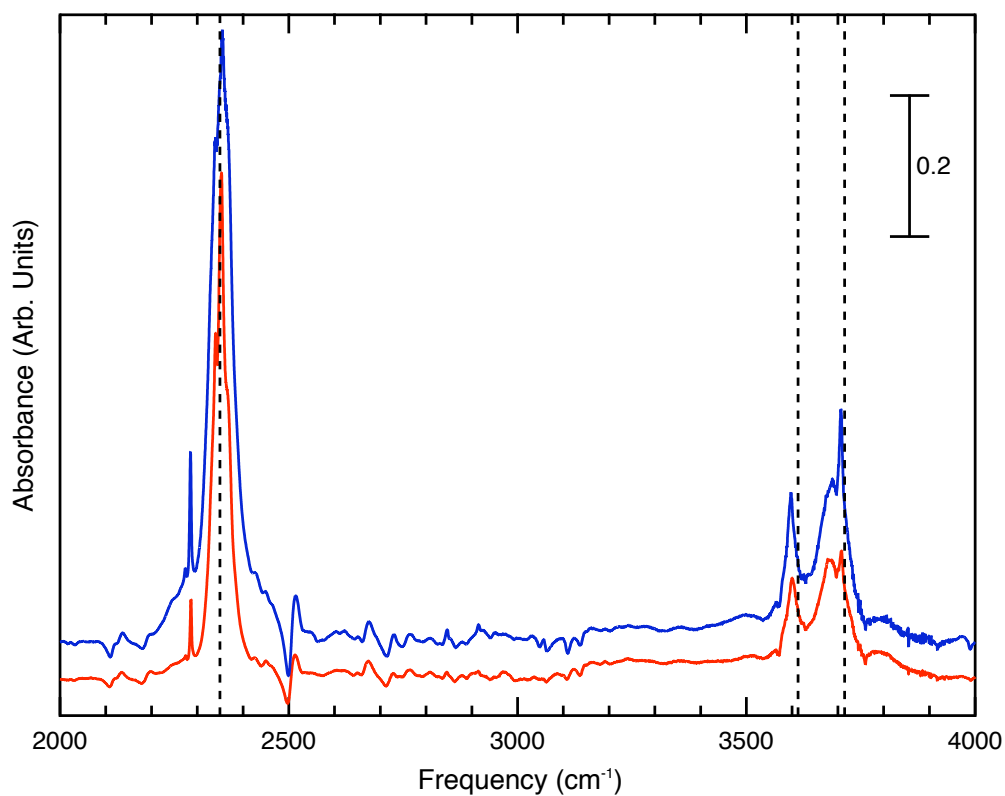
Figure 6.1: Full absorbance spectra of CO_2 in Mg-MOF-74 - The red trace corresponds to a concentration of 0.21 CO_2 per open Mg site; the blue trace corresponds to 0.50 CO_2 per Mg site. Dashed lines indicate gas-phase, pure vibrational (Q(0)) values of the ν_3 transition (2349 cm^{-1}) and the $\nu_1 + \nu_3$ and $2\nu_2 + \nu_3$ Fermi resonance combination transitions (3613 cm^{-1} and 3715 cm^{-1}). Spectra have gas-phase peaks subtracted off and are offset for clarity. Data were taken on 2/18/2011.

resonance of the ν_1 fundamental and $2\nu_2$ overtone transitions. While keeping in mind that in reality the two frequencies in the 3500-3800 cm^{-1} region result from a linear combination of the two transitions, we will refer to the dashed line in the figure at 3613 cm^{-1} as the $2\nu_2 + \nu_3$ transition and the line at 3715 as the $\nu_1 + \nu_3$ transition for ease in referring to the bands independently.

Bands due to the Fermi resonance of the ν_1 and $2\nu_2$ transitions do not appear in our spectra. Both transitions are symmetric in free CO_2 and thus lack nonzero transition dipole-moment matrix elements, making them infrared-inactive. They are only active when occurring in combination with the asymmetric-stretch (ν_3) transition. However, as discussed in § 3.1, interaction of the adsorbed molecule with the MOF could perturb the molecule's wavefunction, inducing a dipole moment significant enough to make these transitions infrared-active. Such a phenomenon allows for infrared absorption bands due to bound H_2, which is infrared-inactive in the gas phase (19). That these bands do not appear in our spectra suggests that this phenomenon may be insignificant for CO_2, although the region in which the bands would occur (1300-1400 cm^{-1}) is nearly outside of the frequency range emitted by our infrared source. Thus there may be weak bands due to the ν_1 and $2\nu_2$ Fermi resonance that are beyond the ability of our apparatus to detect. If these bands exist, they lie below the noise level in that region of our spectra. The confirmation that these transitions do or do not occur we leave as a topic for future study.

In Fig. 6.2 we show infrared spectra of gas-phase CO_2 at a variety of concentrations. Rovibrational peaks in the 2200-2500 cm^{-1} and the 3500-3800 cm^{-1} regions are visible. Inset are zoomed-in plots of the two regions in which bands appear. The left inset plot shows rotational sidebands surrounding the central Q(0) (pure vibrational) transition frequency of the ν_3 mode, which, as discussed in § 2.5, is quantum-mechanically forbidden. The right inset plot shows rotational sidebands of the $2\nu_2 + \nu_3$ and the $\nu_1 + \nu_3$ combination transitions with Q-frequencies marked by dashed lines. The gas-phase rovibrational bands are very sharp and are unresolved in our 0.5-cm^{-1}-resolution spectra, and even at 0.1 cm^{-1} resolution, the bands are still not fully resolved.

In the adsorbed-CO_2 spectra, we do not see rotational side bands, which is consistent with neutron-diffraction data and indicates that the bound molecules cannot rotate freely (29). Instead a single or a few peaks appear that are due to pure vibrational transitions in CO_2. Recall from § 2.5 that the restriction for free CO_2 prohibiting
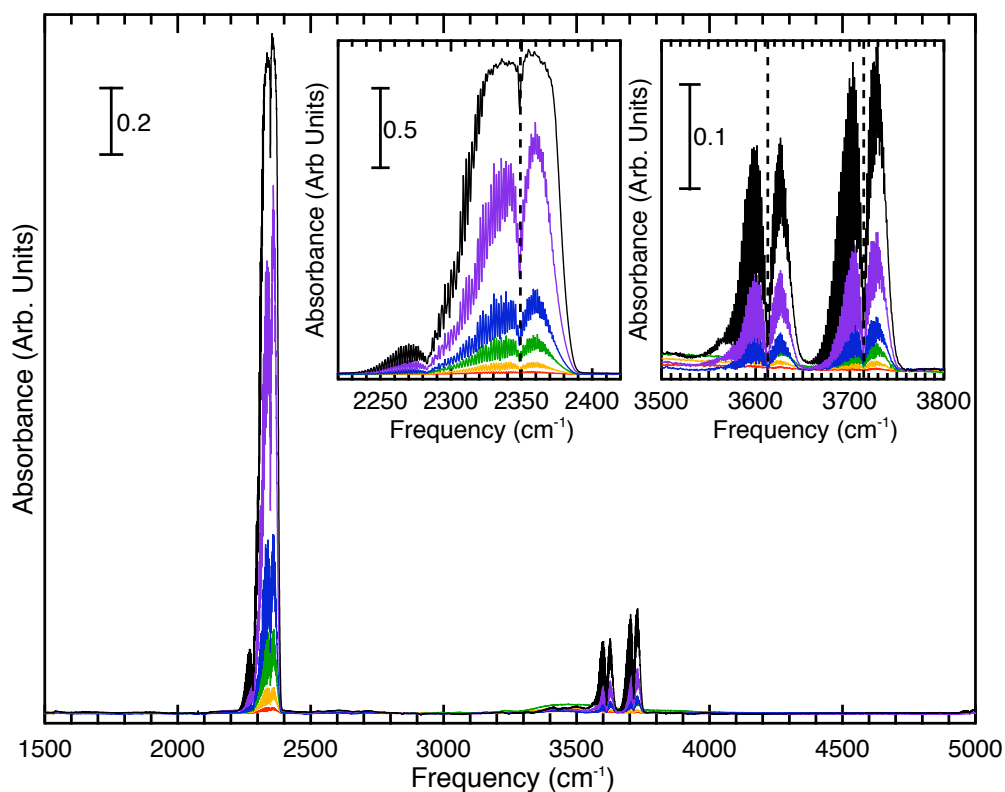
Figure 6.2: Infrared spectra of gas-phase carbon dioxide. - From bottom to top, spectra were taken at pressures of 5.8, 27, 81, 167, 423, and 940 mbar, all at 0.5 cm^{-1}. Inset are zoomed-in plots of the two regions where rovibrational bands appear. The left inset plot shows the rotational sidebands of the ν_3 vibrational transition. The central Q-frequency, which is quantum-mechanically forbidden, is marked by the dashed line. The right inset plot shows the rotational sidebands of the $2\nu_2 + \nu_3$ and $\nu_1 + \nu_3$ combination transitions with Q-frequencies marked by dashed lines. Data were taken on 2/23/2011.

transitions, in which only the vibrational quantum number of the molecule changes, is lifted in the adsorbed phase. An infrared photon can cause simultaneous transitions in the molecule and in the host framework that balance the sign of the wavefunction describing the system.

In the following section we examine the asymmetric stretch (ν_3) peaks of adsorbed CO_2 in Mg-MOF-74 and compare them to equivalent peaks of CO_2 in other members of the MOF-74 isostructural series.

6.2 Asymmetric stretch of CO_2

Here we focus on the ν_3 transition of adsorbed CO_2 in Mg-MOF-74 as compared to Mn-, Co-, and Zn-MOF-74. We identify the adsorbed-phase bands and discuss their shifts with temperature and concentration. Figure 6.3 displays the ν_3 region of spectra of adsorbed CO_2 in Mg-MOF-74 at low equilibrium pressures, all below 3 mbar and all corresponding to concentrations less than 0.2 CO_2 per Mg. All peaks that appear are given in Table 6.1 and are labeled either 1, 2, or 3.

Table 6.1: Frequencies of CO_2 ν_3 peaks in Mg-MOF-74 –Values are given to the nearest half-cm^{-1}

Isotopologue	Gas Phase	Peak 1	Peak 2	Peak 3
$^{12}C^{16}O_2$	2349	2352.5	2340.5	2367.5
$^{13}C^{16}O_2$	2283.5	2286	2275	–

The smaller peaks numbered 1 and 2 are due to the ν_3 transition in the $^{13}C^{16}O_2$ isotopologue, which occupies 1% of naturally occurring CO_2. In § 6.2.4 we will analyze these bands further and justify their designation as belonging to $^{13}C^{16}O_2$.

Focusing on the main $^{12}C^{16}O_2$ bands in the 2300-2400 cm^{-1} region, we have labeled the peaks 1, 2, and 3 for clarity. Peak 1 refers to the central, highest intensity absorption peak of trapped CO_2. Peak 2 is the left shoulder redshifted from peak 1 by 12 cm^{-1}. Peak 3 is the right shoulder blueshifted from the main peak by 15 cm^{-1}. In § 6.2.2 we will discuss the origins of peaks 2 and 3 as contrasted with peak 1.
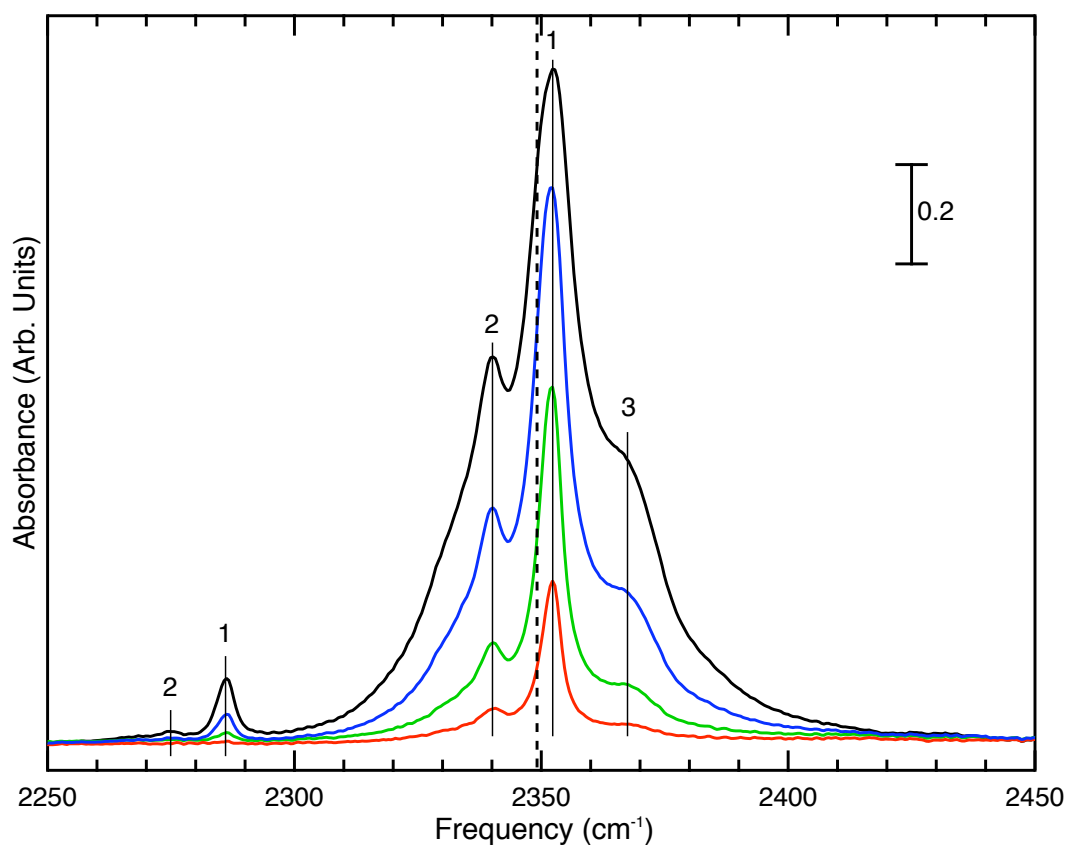
Figure 6.3: Asymmetric stretch (ν_3) region of adsorbed CO_2 in Mg-MOF-74 - Spectra were taken at $1\,\mathrm{cm}^{-1}$ resolution at ambient temperature and decreasing equilibrium pressure. From top to bottom, spectra were taken at 2.6 mbar, 0.9 mbar, 0.2 mbar, and base pressure (<0.1 mbar), all of which correspond to concentrations of adsorbed CO_2 of less than 0.2 CO_2/Mg. The dashed line marks the gas-phase ν_3 frequency. The smaller peaks numbered 1 and 2 are due to the $^{13}C^{16}O_2$ transition; the larger peaks numbered 1, 2, and 3 are associated with $^{12}C^{16}O_2$. Data were taken on 12/10/2011.

6.2.1 Blueshift in Mg-MOF-74

Here we discuss the frequency shift upon adsorption of the ν_3 transition of carbon dioxide, focusing on the central, highest intensity band, which we have termed peak 1. The band corresponds to the CO$_2$ adsorbed to the primary binding site in Mg-MOF-74, which neutron diffraction data confirm is next to the open metal (29). This primary site peak is blueshifted from the gas-phase ν_3 transition by approximately 4 cm^{-1}, although the shift depends on the concentration of adsorbed CO$_2$, as we will discuss in § 6.4.

Figure 6.4 shows spectra of adsorbed CO$_2$ in four members of the MOF-74 isostructural series. From top to bottom, the traces correspond to CO$_2$ in the magnesium, manganese, cobalt, and zinc compounds. The Mg-MOF-74 spectrum was taken at base pressure; all loaded CO$_2$ was adsorbed. The Mn-MOF-74 spectrum was taken at an equilibrium pressure of 48 mbar, and the Co- and Zn-MOF-74 spectra were taken at equilibrium pressures of 58 and 77 mbar respectively. All spectra were taken at 1-cm^{-1} resolution.

The higher CO$_2$-signal in the Mg-MOF-74 sample at lower equilibrium pressure as compared to the Mn- Co- and Zn-MOF-74 samples is a result of the higher CO$_2$ binding energy of the Mg compound with respect to the other compounds. At equivalent pressures, there is a higher concentration of adsorbed CO$_2$ in the Mg sample than in the other samples.

The spectra of CO$_2$ in the four compounds have similar features. Each clearly has a central, highest intensity peak shaped like the Mg-MOF-74 trace's peak 1 and a left shoulder shaped like the band we termed peak 2. The principle difference among the spectra are the frequency shifts of the adsorbed peaks relative to the gas-phase frequency. As is shown in Table 6.2, the frequency of the main, highest intensity peak is redshifted with respect to the gas-phase asymmetric stretch transition in the Mn-, Co-, and Zn-MOF-74 materials, whereas it is blueshifted in Mg-MOF-74.

The precise mechanism behind the blueshift in Mg-MOF-74 is unknown. Theoretical calculations reported by Wu et al. predict a redshift in the ν_3 transition of CO$_2$ upon adsorption to Mg-MOF-74. A redshift upon adsorption is more common than a blueshift. In the as of yet unpublished paper by FitzGerald et al. on MOF-74 binding sites for molecular hydrogen, the vibrational frequency redshift for adsorbed H$_2$
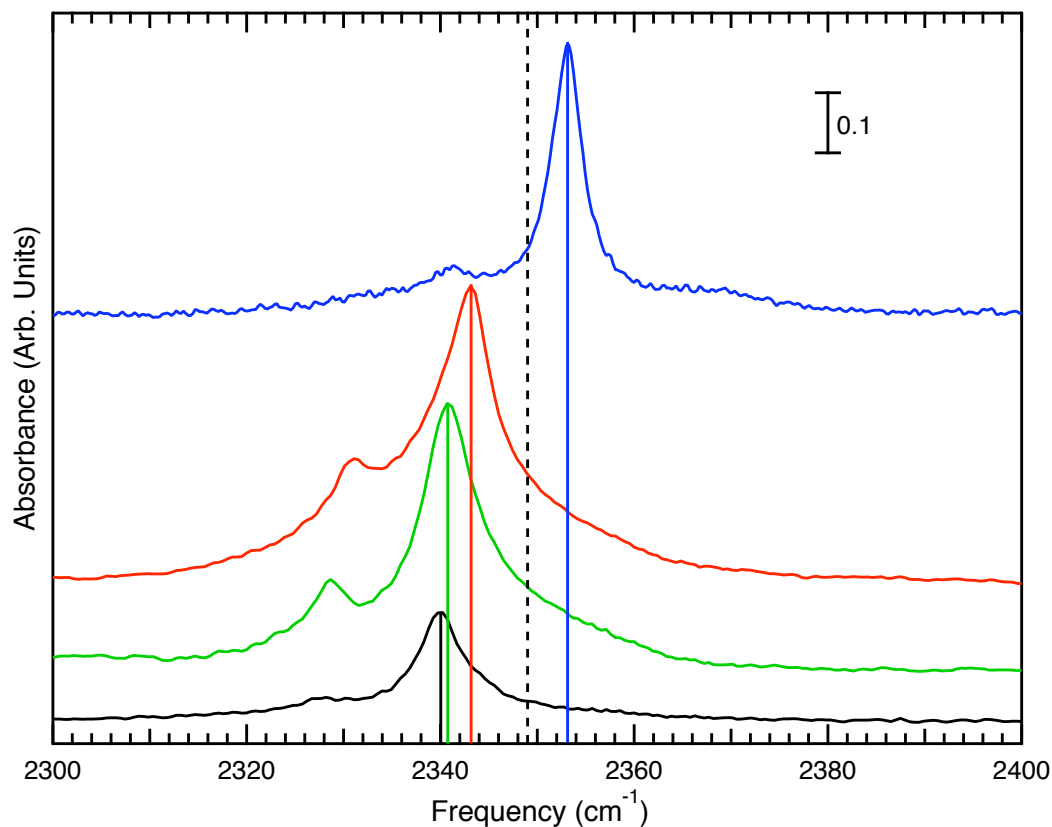
Figure 6.4: Absorbance spectra of ν_3 transition of CO_2 in the isostructural series - From top to bottom, the traces correspond to CO_2 in the magnesium, manganese, cobalt, and zinc compounds. The dashed line at 2349 cm^{-1} marks the gas-phase CO_2 asymmetric-stretch transition frequency. The Mg-MOF-74 spectrum was taken at base pressure; all loaded CO_2 was adsorbed. The Mn spectrum was taken at an equilibrium pressure of 48 mbar, and the Co and Zn spectra were taken at equilibrium pressures of 58 and 77 mbar respectively, all of which correspond to concentrations of less than 0.2 CO_2/Mg. All spectra were taken at 1 cm^{-1} resolution and are offset for clarity.

Table 6.2: Frequencies of CO$_2$ ν_3 peaks in M-MOF-74–Values are given to the nearest cm^{-1}

M	Frequency	Shift
(gas phase)	2349	-
Mg	2353	4
Mn	2343	-6
Co	2341	-8
Zn	2340	-9

is found to correlate with binding energy. Adsorbed CO$_2$ clearly bucks this trend, as Mg-MOF-74 is the most strongly binding species for carbon dioxide. However, the vibrational peaks due to hydrogen in the Mg-MOF-74 primary site are less redshifted than the trend would suggest. This discrepancy is consistent with that observed in our adsorbed CO$_2$ spectra. FitzGerald et al. speculate that the inconsistency could be a reflection of magnesium's smaller cationic size relative to the other metals in the series (36).

Many literature sources have reported a blueshift of the CO$_2$ asymmetric-stretch transition frequency upon interaction with adsorbents (33, 41, 42). In particular, Valenzano et al. have published IR data on adsorbed CO$_2$ in Mg-MOF-74 and report the same 4 cm^{-1} blueshift we observe (43). Although they report that the blueshift agrees with computational calculations, they offer no physical explanation for its origin. Zhou et al., in studies of CO$_2$ adsorbed to metal ions attribute their observed blueshift in the ν_3 transition to the electrostatic character of the interaction (41). They offer no further explanation however. In a paper on IR spectroscopy of Fe$^+$-(CO$_2$)$_n$ clusters, Gregoire and Duncan attribute a blueshift in the ν_3 frequency to increased repulsion from the metal as the oxygen vibrates against it (42). In another paper on metal-CO$_2$ clusters, Gregoire et al. attribute observed blueshift to increased repulsion on the inside potential wall due to the metal ion (33).

As follows from the interaction frequency shift analysis in § 3.2, increased repulsion on the vibrational potential walls corresponds to a positive value of $\langle U_1' \rangle_0$, which can lead to a blueshift. Therefore, it seems likely that Gregoire's explanation for blueshift applies to the ν_3 transition of CO$_2$ adsorbed to Mg-MOF-74. The redshifts in the other three compounds suggest that the repulsive interaction between CO$_2$ and the other

metals is less.

We do not attempt to offer an explanation here for what feature of the magnesium compound in particular causes this increased repulsion. It may be related to the magnesium ion's smaller size with respect to the other metals in the series, as FitzGerald et al. surmise (36). The CO_2 may bind slightly closer to the Mg than to the other larger metals, which could lead to more overlap of the electronic wavefunctions associated with the molecule and the exposed metal. More wavefunction-overlap can produce more repulsion as a result of quantum-mechanical antisymmetry requirements (19). This phenomenon is very difficult to model; thus it is difficult to predict the strength of the repulsion from the identity of the host material.

6.2.2 Band identification

The spectra of CO_2 in the four compounds have similar features. Each clearly has a central, highest intensity peak and a left shoulder shaped like peaks 1 and 2 in the Mg-MOF-74 spectra. We use the name peak 1 to refer to the central band in each MOF-74 species, and we attribute the band to CO_2 in its primary binding site and preferred orientation in the framework, bound end-on next to the exposed metal, as shown in neutron diffraction data (29). We attribute the left shoulder feature in each MOF, which we call peak 2 for all MOFs in the series, to CO_2 in a different location or configuration with respect to the framework.

Dietzel et al. and Valenzano et al. display spectra of the ν_3 bands of adsorbed CO_2 in Ni-MOF-74 and Mg-MOF-74 respectively. Both sets of spectra show the same shoulder band that we have called peak 2 (11, 43). Dietzel et al. attribute both peaks 1 and 2 to CO_2 occupying the primary binding site by the exposed metal.

In the following paragraphs we justify the conclusion that peak 2 arises from CO_2 in the primary site, just like peak 1. We further speculate on possible origins for the 12 cm^{-1} difference between the frequencies of the two peaks.

We begin by considering a range of possible explanations for the origin of peak 2 and rule out explanations that are incompatible with our results, while keeping in mind that there may exist other explanations that we have not considered. Possible origins of peak 2 are as follows: it could arise from CO_2 occupying a secondary site in the framework; it could arise from CO_2 in the same primary site that leads to peak 1 but

in a slightly different orientational configuration; it could arise from bound CO$_2$-CO$_2$ interactions; it could arise from librational or translational sidebands.

Even though none of the CO$_2$ concentrations reported are above one adsorbed CO$_2$ molecule per primary site, it is still possible that bands due to less-energetically-favorable secondary sites could appear in our spectra. At ambient temperatures, at which the majority of out spectra were taken, entropic effects become important and allow for less energetically favorable sites to begin to fill before all primary sites are completely occupied. Therefore, we cannot use a low-concentration argument to rule out a secondary site as the cause of peaks 2 and 3.

We rely on the results found by FitzGerald et al. to conclude that peak 2 does not arise from carbon dioxide occupying a secondary site in a different location in the framework cell (36). In spectroscopic studies of molecular hydrogen in the MOF-74 series, the frequency of the peaks due to hydrogen in the primary binding site shift upon substitution of coordination metal, whereas the secondary site peaks remain essentially fixed. Neutron studies indicate that the primary binding site for H$_2$ in MOF-74 is next to the exposed metal whereas secondary sites are farther away from the metal(17). FitzGerald et al. conclude that the proximity of the primary site to the metal explains the dependence of the measured frequency shift on the metal's identity, whereas secondary sites are far enough away from the metal such that the vibrational frequency shifts are virtually unaffected by the identity of the metal.

In spectra of CO$_2$ in the MOF-74 series, as shown in Fig. 6.4, peaks 1 and 2 shift the same amount upon metal substitution. Table 6.3 gives the shift of peak 2 relative to peak 1, which is consistently -12 cm^{-1} across the series, indicating that the two peaks must be due to carbon dioxide with the same center of mass location relative to the MOF. In particular they are both due to CO$_2$ occupying the primary, open metal site, as their frequency shifts depend on the identity of the coordination metal.

Spectra taken at a range of temperatures aid us in narrowing down the possible origins of peak 2. Figure 6.5 displays temperature dependent spectra of the ν_3 CO$_2$ bands in Mg-MOF-74. At low concentration (0.025 $\pm$ 0.005 CO$_2$ molecules per open metal site), peak 2 appears as a discrete band at 2341 cm^{-1}. As the system cools, the band shrinks, and it disappears below the noise level at roughly 100K. Peak 1, at 2353 cm^{-1}, sharpens with cooling. At 65K a distinct right shoulder appears at 2355 cm^{-1}. We discuss the origin of this right shoulder band in the following section.
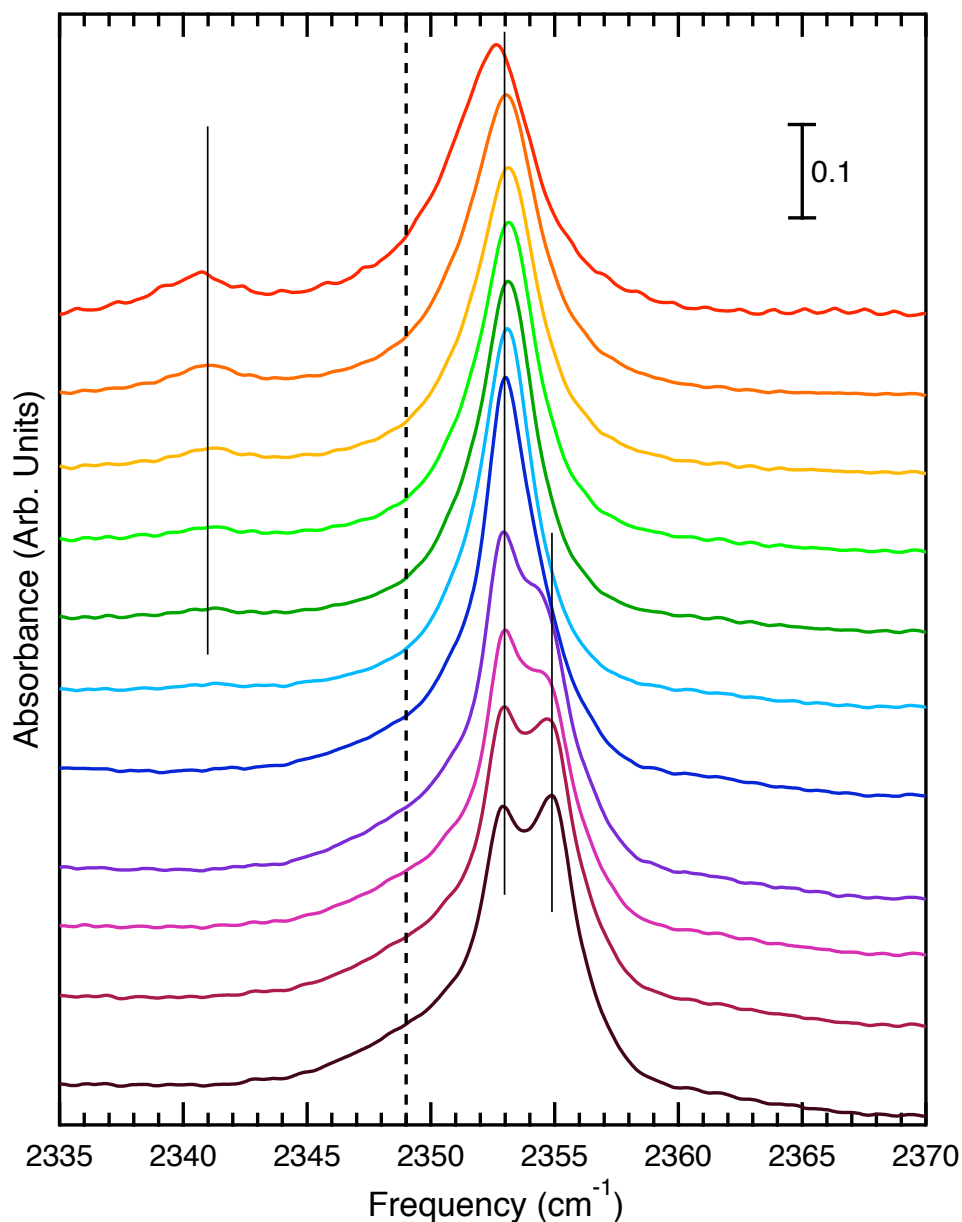
Figure 6.5: Temperature dependence of ν_3 bands of CO_2 in Mg-MOF-74 - Spectra were taken at 0.5 cm^{-1} resolution as the system cooled at a concentration of 0.025 ± 0.005 CO_2 per open metal site. From top to bottom, traces correspond to spectra taken at 303K, 251K, 222K, 193K, 163K, 133K, 104K, 75K, 65K, 54K, 44K, and 34K. The dashed line represents the gas-phase ν_3 transition; the solid lines mark the central frequencies of the adsorbed CO_2 peaks. Data were taken on 1/20/2011.

If peak 2 arose from a perturbation to the potential energy well of CO$_2$ in its primary binding site due to interactions with CO$_2$ molecules in adjacent sites, then for peak 2 to disappear upon cooling, molecules would have to migrate to sites farther away from one another at low temperatures. On the timescale of our experiments, however, we observe that the molecules are frozen into their sites below 200K and do not migrate. Thus, CO$_2$–CO$_2$ interactions cannot explain the difference between the origins of peak 2 and peak 1. In § 6.4, we discuss features in our spectra that can be attributed to CO$_2$–CO$_2$ interactions.

The shrinking of peak 2 with decreasing temperature suggests that peak 2 corresponds to a configuration of the molecule in the framework that is less energetically favorable than that which causes peak 1. Since the bound molecule cannot migrate to different sites, the transitions corresponding to peak 2 may arise from molecules at a slightly different angle with respect to the metal, or molecules at a slightly different center-of-mass position within the primary site. The potential well for bound CO$_2$ may have two local minima at slightly different energies, corresponding to two different orientations or positions with respect to the metal. Vibrational transitions while the molecule is in one configuration may differ from transitions in which the molecule is in the other configuration.

A slightly different possible explanation does not require the existence of a potential well with two local minima. Wu et al. report that their neutron diffraction measurements indicate that CO$_2$ bound to Mg-MOF-74 can occupy a range of angular orientations with respect to the metal (29). At high temperatures they report that the orientational disorder increases. In other words, the CO$_2$ populates more excited librational levels. It is possible that peaks 1 and 2, correspond to two transitions, one in which the molecule remains in a librational ground state and one in which it remains in a librational excited state. This phenomenon would be analogous to vibrational transitions of ortho and para hydrogen (20).

In hydrogen there exist peaks corresponding to $\Delta J = 0$ vibrational transitions in which the initial state has $J = 1$ (ortho hydrogen) and $\Delta J = 0$ transitions in which the initial state has $J = 0$ (para hydrogen). The energy spacings between these two transitions differ slightly from one another, such that there is a 6 cm^{-1} difference between the peaks.

It is plausible that a similar phenomenon may be leading to the 12 cm^{-1} difference between the frequencies of peaks 1 and 2. If, at room temperature, bound CO_2 occupies two different librational states, one of lower energy than the other, then pure vibrational transitions in which the molecule remains in its ground librational state may differ by 12 cm^{-1} from transitions in which it remains in the second, higher-energy librational state. The temperature-dependent data would allow us to assign peak 2 to carbon dioxide in the librationally excited state undergoing a pure vibrational transition. As the temperature decreases, this excited state becomes depopulated, and peak 2 disappears.

Knowledge of librational energy spacings would aid in classifying peak 2 with more certainty.

Table 6.3: Frequences in cm^{-1} of CO_2 ν_3 peaks in M-MOF-74

M	Peak 2	Shift from Peak 1
Mg	2341	-12
Mn	2331	-12
Co	2329	-12
Zn	2328	-12

Analysis similar to that used for identifying the origin of peak 2 may be applied to the right shoulder band that we have named peak 3. However, present data is insufficient for such an analysis, as the temperature-dependent spectra and the spectra taken in the other MOF-74 species have CO_2-concentrations that are too low for peak 3 to be visible. The characterization of peak 3 will be left as a topic for future work.

6.2.3 Low-temperature bands and shifts

Figure 6.5 shows that as the temperature decreases, a band at 2355 cm^{-1} becomes resolved as distinct from the 2353 band cm^{-1} we have called peak 1. Curve fits suggest that both overlapping peaks exist even at high temperatures and sharpen upon cooling, such that the doublet is visible. However, the sharpening effect alone is not enough to explain the appearance of the 2355 cm^{-1} band. This band grows significantly with decreasing temperature, while the 2353 cm^{-1} band decreases in intensity. The temperature dependence of the band intensities indicate that they arise from CO_2 molecules experiencing different conditions in the MOF. Just as with peak 2, the 2355 cm^{-1} band, which we will call peak 1a, likely arises from a slightly different configuration of CO_2 in

its primary site. We conclude that the configuration leading to peak 1a is slightly more energetically favorable than the configuration leading to peak 1. The energy difference ΔE between the two configurations is only significant at temperatures for which the value of $k_B * T$ is comparable to ΔE, with k_B being the Boltzmann constant and T the temperature in Kelvin. At higher temperatures (above 100K), entropic effects dominate and the the configuration producing peak 1a is no longer preferred over that producing peak 1.

Comparing the intensities of the two bands, that is, the areas under the curves, at a range of temperatures allows us to extract a rough measurement for ΔE between the configurations. We fit the bands to Lorentzian functions and find the areas A_1 and A_{1a} underneath them. The ratio of these intensities is proportional the the ratio of the populations P_1 and P_{1a} of the two configurations,

$$\frac{A_1}{A_{1a}} \propto \frac{P_1}{P_{1a}}. \tag{6.1}$$

Thus we can relate the ratio of areas to ΔE via the Boltzmann factor,

$$\frac{A_1}{A_2} \propto e^{-\Delta E/k_B T} \tag{6.2}$$

Applying the natural logarithm to both sides of the equation yields

$$\ln\left(\frac{A_1}{A_2}\right) \propto \frac{\Delta E}{k_B}\left(\frac{1}{T}\right) \tag{6.3}$$

Thus, by plotting the natural log of the ratio of the areas under the curves against the reciprocal of temperature, we can extract ΔE. Figure 6.6 shows such a plot, called an Arrhenius Law plot, for the intensities of peaks 1 and 1a. The spectra from which the areas were calculated were taken at a concentration of 0.1 ± 0.05 CO$_2$/Mg at temperatures ranging from 30 to 100 K. Using a concentration this low allows for the peaks to be narrow enough that they are distinguishable from one another. In Fig. 6.6(a), the blue trace that slopes upward with increasing temperature marks the intensity A_1 of peak 1. The red trace represents the intensity A_{1a} of peak 1a. The slope of the linear fit in Fig. 6.6(b) gives a difference in binding energy between the two configurations of 80 ± 10K, or 0.7 ± 0.1 kJ/mol.

We were unable to apply this Arrhenius-Law analysis to find the energy difference between the configurations leading to peaks 1 and 2 because the shape of the features
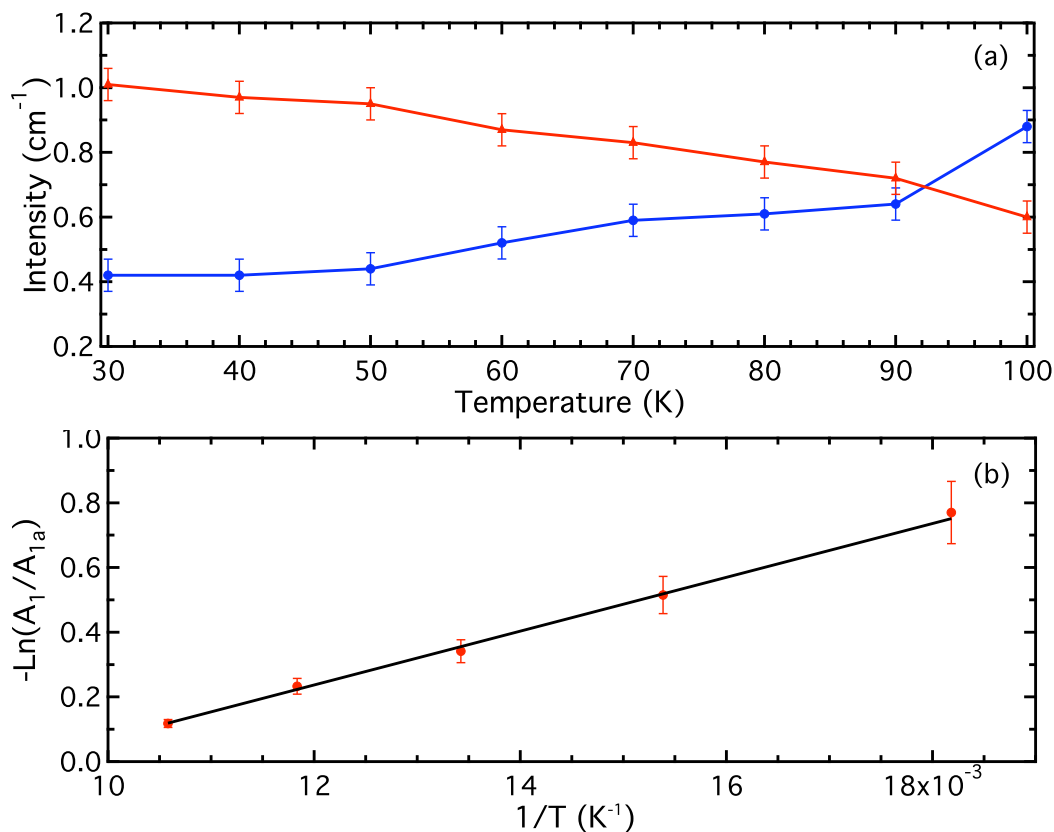
Figure 6.6: Temperature dependence of peak intensities - Intensities of bands at 2353 and 2355 cm^{-1} plotted against temperature are given in (a). The blue trace that slopes upward with temperature represents the intensity A_1 of the 2353 band (peak 1); the red trace represents the intensity A_{1a} of the 2355 band (peak 1a). The intensities were calculated via fitting the overlapping bands to Lorentzian curves. In (b) is an Arrhenius Law plot based on the same peak intensities A_1 and A_{1a} over the temperature range 50-90K. The slope of the linear fit in (b) gives a difference in binding energy between the two configurations of 80 ± 10K, or 0.7 ± 0.1 kJ/mol. Spectra were taken on 1/24/2011.

in the ν_3 region complicated curve-fitting. The region in which peaks 1, 2, and 3 appear likely contains other broader, overlapping bands. Fitting to three curves produced poor fits, yet fitting to more than four curves required more free parameters than we could justify.

In addition to the appearance of peak 1a with decreasing temperature, visible bands also blueshift slightly upon cooling. This phenomenon can be attributed to temperature-dependent contraction of the MOF-lattice, which leads to minor changes in the nature of the interaction with the adsorbed CO_2.

6.2.4 Isotopologue bands

Bands due to the ν_3 transition in the $^{13}C^{16}O_2$ isotopologue appear near the gas-phase $^{13}C^{16}O_2$ frequency. Peak frequencies are given in Table 6.1. At high CO_2 concentrations the peaks due to the more abundant $^{12}C^{16}O_2$ isotopologue saturate, We can analyze the features of high-CO_2-concentration spectra by studying the $^{13}C^{16}O_2$ bands.

As the concentration increases, the $^{13}C^{16}O_2$ peaks 1 and 2 increase in intensity and then level off, suggesting saturation of the primary open metal site. With increasing concentration, the intensity of peak 2 may increase slightly relative to peak 1's intensity. However, the increase is too small to lie outside of the associated uncertainty in the measured intensities.

Table 6.4: Frequencies in cm^{-1} of ν_3 peaks of $^{13}C^{16}O_2$ in Mg-MOF-74 at two characteristic CO_2 concentrations-Frequency shifts at increased concentrations are due to CO_2–CO_2 interactions.

Peak #	Frequency at 0.21 CO_2/Mg	Frequency at 1.0 CO_2/Mg	Shift
1	2286.2 cm^{-1}	2284.8 cm^{-1}	1.4 cm^{-1}
2	2274.6 cm^{-1}	2273.9 cm^{-1}	0.7 cm^{-1}

6.3 High-frequency region

In the high frequency region of 3500-3800 cm^{-1}, two large peaks appear at 3597 cm^{-1} and 3706 cm^{-1} that grow with increasing CO_2 concentration, as displayed in Fig. 6.8. We attribute these bands to the transition due to the Fermi resonance of the combination $\nu_1 + \nu_3$ and $2\nu_2 + \nu_3$ transitions, where $2\nu_2$ is the overtone transition of the bending
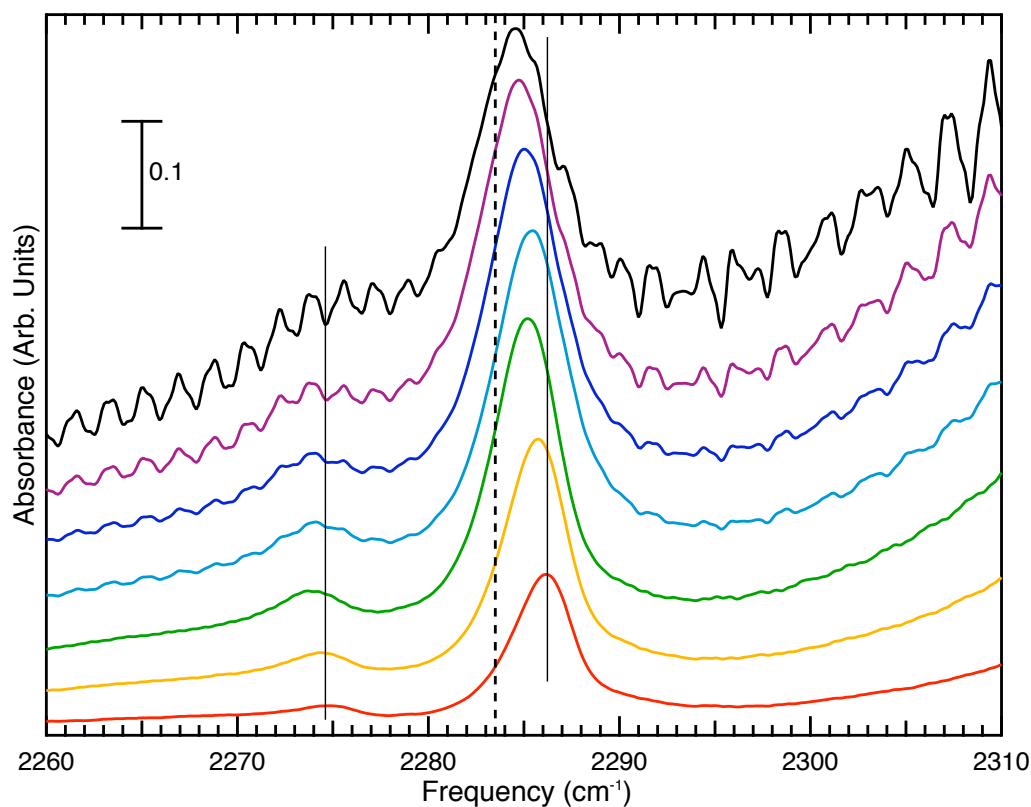
Figure 6.7: Concentration dependence of ν_3 band of $^{13}C^{16}O_2$ in Mg-MOF-74 - From bottom to top, spectra correspond to concentrations of 0.21, 0.35, 0.50, 0.63, 0.73, 0.84, and 1.0 CO_2 per open Mg site. The dashed line represents the gas phase ν_3 transition frequency for $^{13}C^{16}O_2$. Adsorbed-phase frequencies and shifts are given in Table 6.4. Spectra are offset for clarity and gas-phase peaks are subtracted off. Data were taken on 2/18/2011.

mode, which occurs at nearly the same energy as the ν_1 transition. Another broader band appears at 3687 cm^{-1} that does not grow with increasing concentration; rather it shrinks slightly. This may also be a $\nu_1 + \nu_3$ transition of adsorbed CO_2.

In the gas-phase CO_2 spectrum, we see two envelopes of peaks corresponding to this vibrational doublet in combination with rotational transitions. The gas-phase, pure-vibrational frequencies have are 3613 cm^{-1} and 3715 cm^{-1} (23). Table 6.5 shows the peak frequencies and the shifts from their respective gas-phase values. Both peaks are redshifted. Further work should include studying the temperature-dependence of these bands, comparing the bands across the isostructural series, and developing an explanation for the redshifts of the bands.

In Fig. 6.8(b) spectra are divided by their CO_2-concentrations, making clear that the peak intensities do not scale with concentration. This effect appears across all of our spectra and we attribute it to the adsorbate molecules not spreading uniformly throughout the sample. Rather, they primarily coat the surfaces at low concentrations. The infrared beam interacts more with the surfaces of the sample crystals than with their interiors. As a result, concentration of CO_2 seen by the infrared radiation is higher than the concentration we measure, because the isotherm method assume even spreading of adsorbate throughout the host. When more CO_2 is added to the system, the molecules fill sites out of the beam's path, such that the concentration does not appear to rise as much in the infrared as our isotherm method would suggest.

Table 6.5: Frequencies in cm^{-1} of combination vibrational transitions of CO_2 in Mg-MOF-74

Modes Excited	Gas Phase Freq.	Adsorbed Phase Freq.	Shift
$2\nu_2 + \nu_3$	3612.84	3600	-13
$\nu_1 + \nu_3$	3714.78	3708	-7
$\nu_1 + \nu_3$	3714.78	3687	-28

6.4 Concentration-dependent frequency shifts

As the concentration of CO_2 increases to one adsorbed molecule per primary site, the bound-CO_2 bands redshift by approximately 1 cm^{-1}. This shift-upon-filling phe-
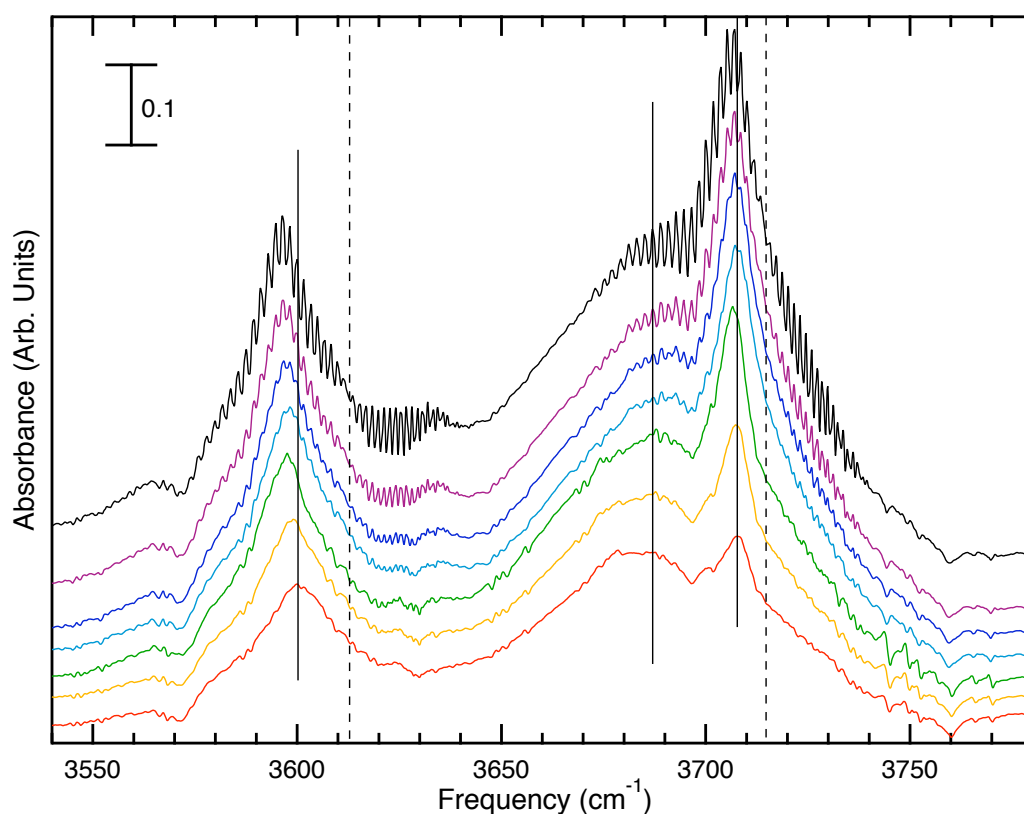
Figure 6.8: Combination vibrational peaks of CO_2 in Mg-MOF-74 - Shown in (a) are the spectra with increasing concentration. Dashed lines represent gas-phase frequencies. From bottom to top, concentrations are 0.21, 0.35, 0.50, 0.63, 0.73, 0.84, and 1.0 CO_2 per open Mg site. In (b) the same spectra are divided by their associated CO_2 concentrations. Spectra are offset for clarity and gas-phase peaks are subtracted off. Data were taken on 2/18/2011.

nomenon has been observed in H_2 data and attributed to interactions among adsorbed CO_2 molecules in nearby sites (36).

As the concentration approaches 1 CO_2 per metal site, the adsorbed molecules are packed closely together. The carbon-to-carbon distance between nearest neighbors is 5.2 Å and the distance to the second-nearest neighbor is 7.03 Å according to neutron-diffraction data (29). These distances are close to the carbon-carbon distance in solid CO_2 of approximately 4 Å. Such close packing in the MOF indicates that at high concentrations the quadrupole moments of the bound CO_2 molecules interact, changing the potential well that each molecule experiences and thus changing the transition frequencies slightly.

6.5   Librations and translations

As mentioned in Chapter 2, bound CO_2 may undergo intermolecular transitions, in which it moves to higher-energy translational or librational levels. We do not see side-bands corresponding to these transitions in our spectra, however. The frequency range in which they are predicted to occur contains many intense MOF bands, which may obscure CO_2-bands. Additionally, librational or translational bands may be smeared out due to slightly different conditions experienced by molecules in different unit cells. Further work should including confirming that librational and translational transitions do or do not occur in spectra of CO_2 in Mg-MOF-74 and, if they do not occur, explaining their absence theoretically.

6.6   Methane in Mg-MOF-74

For the sake of comparison to bound carbon dioxide, we show spectra of the ν_3 transition of CH_4 adsorbed to Mg-MOF-74. Figure 6.9 shows spectra taken, from top to bottom, at 150K, 200K, and 300K and concentrations all less than 0.3 CH_4 per Mg. Sharp bands are gas-phase rovibrational transitions.

The broad band at 3001 cm^{-1} corresponds to the ν_3 transition of adsorbed-phase CH_4. The band is much weaker and broader than CO_2 ν_3 bands and does not appear at temperatures above 150K. We attribute the broadening to greater rotational freedom of the adsorbed CH_4 molecule as compared to adsorbed CO_2. A redshift of -16 cm^{-1}
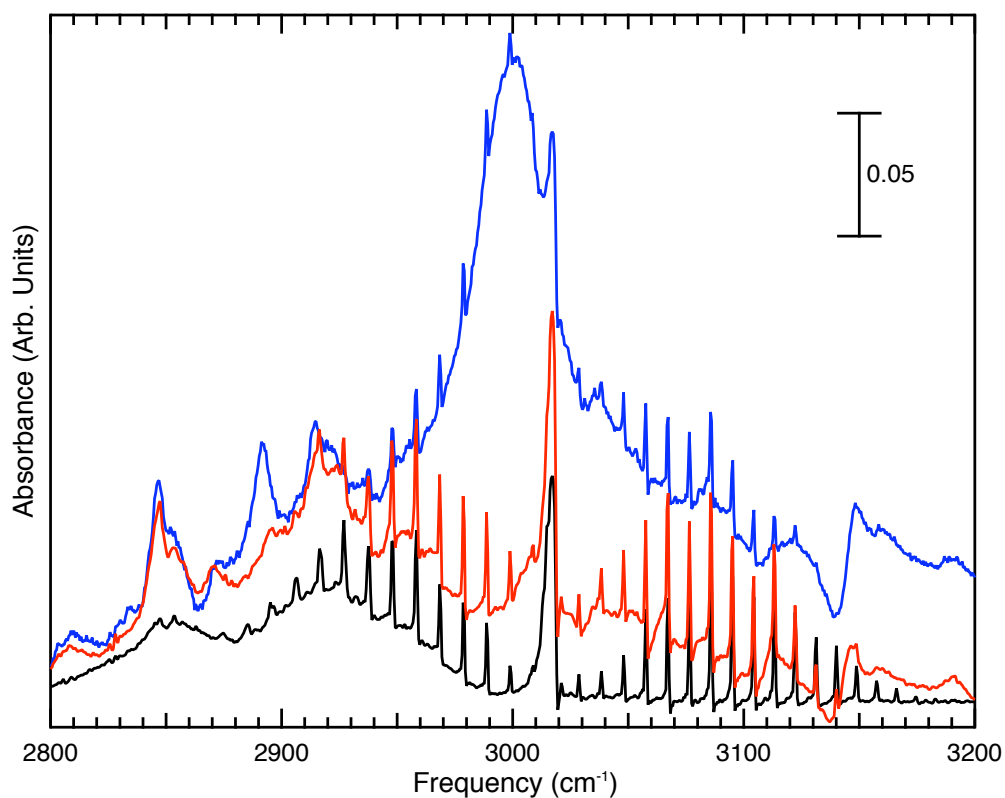
Figure 6.9: Gas-phase and adsorbed-phase CH$_4$ in Mg-MOF-74: ν_3 transition - From top to bottom, spectra correspond to 150K, 200K, and 300K and concentrations all less than 0.3 CH$_4$ per Mg. Sharp bands are gas-phase rovibrational transitions. The broad band at 3001 cm^{-1} corresponds to the ν_3 transition of adsorbed-phase CH$_4$. Data were taken on 2/28/2011.

is observed from the gas-phase ν_3 transition frequency of 3017, which suggests that the mechanism inducing the blueshift in the CO_2 has a significantly weaker effect on CH_4. Future work should include further characterization of the adsorbed methane infrared spectrum in the MOF-74 series.

7

Conclusion

Data collected show a primary binding site for CO_2 in Mg-MOF-74 that leads to blueshifted frequencies of the asymmetric-stretch fundamental transition. The blueshift is unique to Mg-MOF-74, and does not appear in Zn-, Co-, or Mn-MOF-74 spectra. It appears likely that the shift is caused by an increased repulsion between the CO_2 and the magnesium ion with which it interacts strongly. However, more study must be done to develop a more rigorous theoretical explanation for the origin of the blueshift and to gain predictive power over what hosts will induce blueshifts in adsorbates.. Combination-mode transitions are redshifted with respect to gas-phase frequencies, indicating that only the asymmetric-stretch transition energy grows upon adsorption of the CO_2 molecule and not the symmetric-stretch or bending-mode transition energies.

Adsorbed CO_2 in its primary site may have several different configurations that lead to smaller peaks in the adsorbed-CO_2 spectra in Mg-MOF-74. We have ruled out other explanations for these bands including secondary sites and CO_2–CO_2 interactions. CO_2–CO_2 interactions do cause a slight shift of ~ 1 cm^{-1} in the observed frequencies.

Adsorbed methane in its primary site in Mg-MOF-74 produces a broad band at 3001 cm^{-1}, which suggests bound CH_4 has more rotational freedom than bound carbon dioxide. The methane peak is redshifted with respect to the gas-phase ν_3 transition frequency, from which we conclude that the mechanism producing the blueshift in the CO_2 transition does not produce a dominating effect on methane.

Suggestions for further work are given throughout Chapter 6. Overall, investigation of CO_2 and CH_4 more fully in the other members of the isostructural MOF-74 series would help confirm trends and better explain features observed in this thesis.

References

[1] United States National Academy of Sciences. *Understanding and Responding to Climate Change*, 2008. 1

[2] A. C. Buchanan, O. J. Schmidt, M. Buchanan, and O. D. Scholl et al. **Technology and applied R&D needs for carbon capture: Beyond 2020**, March 2010. 1, 2, 4

[3] P. D. C. Dietzel, V. Besikiotis, and R. Blom. **Application of metal-organic frameworks with coordinatively unsaturated metal sites in storage and separation of methane and carbon dioxide**. *J. Mater. Chem.*, **19**:7362–7370, 2009. 1

[4] U.S. Dept. of Energy: Office of Science. *Our Energy Challenges: Council of Energy Research and Education Leaders*, January 20 2010. 2

[5] A. U. Czaja, N. Trukhan, and U. Müller. **Industrial applications of metal-organic frameworks**. *Chem. Soc. Rev.*, **38**:1284, 2009. 2

[6] L. J. Murray, M. Dincă, and J. R. Long. **Hydrogen storage in metal-organic frameworks**. *Chem. Soc. Rev.*, **38**:1294–1314, 2009. 2, 3, 23

[7] J. L. C. Rowsell, A. R. Millward, K. S. Park, and O. M. Yagui. **Hydrogen sorption in functionalized metal-organic frameworks**. *J. Am. Chem. Soc.*, **126**:5666, 2004. 2, 3

[8] J. L. C. Rowsell and O. M. Yagui. **Strategies for hydrogen storage in metal-organic frameworks**. *Angew. Chem. Int. Ed.*, **44**:4670, 2005. 2, 3

[9] N. Rosi, J. Kim, M. Eddaoudi, B. Chen, M. O'Keeffe, and O. M. Yagui. **Rod packings and metal-organic frameworks constructed from rod-shaped secondary building units**. *J. Am. Chem. Soc.*, **127**:1504, 2005. 2, 23, 26

[10] U. S. Department of Energy. **Multi-Year Research, Development and Demonstration Plan: Planned Program Activities for 2005-2015**. 2009. 2

[11] P. D. C. Dietzel, R. E. Johnsen, H. Fjellvåg, S. Bordiga, E. Groppo, S. Chavan, and R. Blom. **Adsorption properties and structure of CO_2 adsorbed on open coordination sites of metal-organic framework Ni_2(dhtp) from gas adsorption, IR spectroscopy, and X-ray diffraction**. *Chem. Commun.*, pages 5125–5127, 2008. 2, 10, 14, 23, 28, 48

[12] J. Hupp, R. Snurr, K. Mulfort, and Y. Bae. **Mixed-ligand metal-organic frameworks for the separation of CO_2 from CH_4** [online, cited March 26, 2010]. 2, 3

[13] P. D. C. Dietzel, B. Panella, M. Hirscher, R. Blom, and H. Fjellvag. **Hydrogen adsorption in a nickel based coordination polymer with open metal sites in the cylindrical cavities of the desolvated framework**. *Chem. Commun.*, pages 959–961, 2006. 3, 27

[14] J. L. C. Rowsell and O. M. Yagui. **Effects of functionalization, catenation, and cariation on the metal oxide and organic linking units on the low-pressure hydrogen adsorption properties of metal-organic frameworks**. *J. Am. Chem. Soc.*, **126**:1304–1315, 2006. 3, 26

[15] Y. Liu, H. Kabbour, C. M. Brown, D. A. Neumann, and C. C. Ahn. **Increasing the density of adsorbed hydrogen with coordinatively unsaturated metal centers in metal-organic frameworks**. *Langmuir*, **24**:4772, 2008. 3, 4, 39

[16] J. G. Vitillo, L. Regli, S. Chavan, G. Ricchiardi, G. Spoto, P. D. C. Dietzel, S. Bordiga, and A. Zecchina. **Role of exposed**

metal sites in hydrogen storage in MOFs. *J. Am. Chem. Soc.*, **130**:8386, 2008. 3, 24

[17] W. Zhou, H. Wu, and T. Yildirim. **Enhanced H_2 adsorption in isostructural metal-organic frameworks**. *J. Am. Chem. Soc.*, **130**:15268, 2008. 3, 4, 24, 26, 27, 49

[18] S. A. FitzGerald, J. Hopkins, B. Burkholder, M. Friedman, and J. L. C. Rowsell. **Quantum dynamics of adsorbed normal- and para-H_2, HD, and D_2 in the microporous framework MOF-74 analyzed using infrared spectroscopy**. *Phys. Rev. B*, **81**(104305), 2010. 3

[19] J. Hopkins. **Infrared spectroscopy of H_2 trapped in metal organic frameworks**, 2009. 3, 13, 41, 48

[20] B. Burkholder. **Catalysis of conversion between the spin isomers of H_2 by MOF-74**, 2009. 3, 51

[21] M. Friedman. **Infrared spectroscopy of adsorbed H_2 in an isostructural series of metal-organic frameworks**, 2010. 3, 13, 14, 24

[22] H. Wu, W. Zhou, and T. Yildirim. **High-capacity methane storage in metal-organic frameworks M_2(dhtp): The important role of open metal sites**. *J. Am. Chem. Soc.*, **131**(13):4995–5000, 2009. v, 4, 24, 27, 28, 30

[23] **HITRAN: Vibrational Modes**, February 2011 [cited March 26, 2011]. 6, 7, 12, 16, 57

[24] D. J. Griffiths. *Introduction to Quantum Mechanics*. Pearson Prentice Hall, 2nd edition, 2005. 10, 14, 18

[25] A. D. Buckingham. **Solvent effects in vibrational spectroscopy**. *Trans. Faraday Soc.*, **56**:753, 1960. 11, 19

[26] I. Suzuki. **General anharmonic force constants of carbon dioxide**. *J. Mol. Spectry.*, **25**:479–500, 1968. 12, 21

[27] P. J. Ogren. **Using the asymmetric stretch band of atmospheric CO_2 to obtain the C=O bond length**. *J. Chem. Ed.*, **79**(1):117–119, 2002. 13

[28] T. Armbruster. **Ar, N_2, and CO_2 in the structural cavities of cordierite, an optical and x-ray single-crystal study**. *Phys. Chem. Mat.*, **12**:233–245, 1985. 13

[29] H. Wu, J. M. Simmons, G. Srinivas, W. Zhou, and T. Yildirim. **Adsorption sites and binding nature of CO_2 in prototypical metal-organic frameworks: A combined neutron diffraction and first-principles study**. *J. Phys. Chem. Lett.*, **1**(13):1946–1951, 2010. 14, 22, 27, 41, 45, 48, 51, 59

[30] G. Herzberg. *Molecular Spectra and Molecular Structure*, **2**. Prentice-Hall, Inc., 1945. 14, 16

[31] *Vibration - Rotation* **Analysis of the Anti-Symmetric Stretch in CO_2**. Montana Tech. 14

[32] M. Vetter, M. Jordan, A. P. Brodyanski, and H. J. Jodl. **IR-Active Matrix-Isolated Molecules (CO and CO_2) to Probe Host Crystal (N_2) Quality**. *J. Phys. Chem. A*, **104**:3698–3711, 2000. 22

[33] G. Gregoire, N. R. Brinkman, D. van Heijnsbergen, H. F. Schaefer, and M. A. Duncan. **Infrared Photodissociation Spectroscopy of $Mg^+(CO_2)_n$ and $Mg^+(CO_2)_n$Ar Clusters**. *J. Phys. Chem. A*, **107**:218–227, 2003. 22, 47

[34] A. R. Millward and O. M. Yagui. **Metal-organic frameworks with exceptionally high capacity for storage of carbon dioxide at room temperature**. *J. Am. Chem. Soc.*, **127**:17998–17999, 2005. 23, 27

[35] S. R. Caskey, A. G. Wong-Foy, and A. J. Matzger. **Dramatic tuning of carbon diozide uptake vis metal substitution in a coordination polymer with cylindrical pores**. *J. Am. Chem. Soc.*, **130**:10870, 2008. 24, 26, 27, 28, 29

[36] S. A. FitzGerald, B. Burkholder, M. Friedman, J. Hopkins, C. J. Pierce, J. M. Schloss, B. Thompson, and J. L. C. Rowsell. **Molecular Hydrogen Binding Sites in MOF-74**. (Unpublished), 2011. 24, 47, 48, 49, 59

[37] D. Britt, H. Furukawa, B. Wang, T. G. Glover, and O. M. Yagui. **Highly efficient separation of carbon dioxide by a metal-organic framework replete with open metal sites**. *Proc. Natl. Acad. Sci. U. S. A.*, **106**(49):20637–20640, December 2009. 28

[38] Z. Bao, L. Yu, Q. Ren, X. Lu, and S. Deng. **Adsorption of CO_2 and CH_4 on a magnesium-based metal organic framework**. *J. Colloid Interface Sci.*, **353**:549–556, 2011. 28

[39] H. Churchill. **Low temperature infrared spectroscopy of H_2 in solid C_{60}**, 2006. v, 33

[40] S. A. FitzGerald, H. O. H. Churchill, P. M. Korngut, and Y. E. Strangas. **Cryogenic apparatus for diffuse reflectace infrared spectroscopy with high-pressure capabilities**. *Rev. Sci. Inst.*, **77**(093110), 2006. 35

[41] M. Zhou, L. Zhang, M. Chen, Q. Zheng, and Q. Qin. **Carbon dioxide fixation by copper and silver halide. Matrix-isolation FTIR spectroscopic and DFT studies of the XMOCO (X=Cl and Br, M=Cu and Ag) Molecules**. *J. Phys. Chem. A*, **104**:10159–10164, 2000. 47

[42] G. Gregoire and M. A. Duncan. **Infrared spectroscopy to probe structure and growth dynamics in Fe^+-$(CO_2)_n$ clusters**. *J. Chem. Phys.*, **117**(5):2120–2130, August 2002. 47

[43] L. Valenzano, B. Civalleri, S. Chavan, G. T. Palomino, C. O. Areán, and S. Bordiga. **Computational and experimental studies on the adsorption of CO, N_2, and CO_2 on Mg-MOF-74**. *J. Phys. Chem. C*, **114**:11185–11191, 2010. 47, 48